Analogue modelling of strain partitioning along a curved strike-slip fault system during backarc-convex orocline formation: Implications for the Cerna-Timok fault system of the Carpatho-Balkanides

Nemanja Krstekanić [a,b,*], Ernst Willingshofer [a], Taco Broerse [a], Liviu Matenco [a], Marinko Toljić [b], Uros Stojadinovic [b]

[a] *Utrecht University, Faculty of Geosciences, Utrecht, the Netherlands*
[b] *University of Belgrade, Faculty of Mining and Geology, Belgrade, Serbia*

ARTICLE INFO

ABSTRACT

Large-scale strike-slip faults are associated with significant strain partitioning in releasing/restraining bends and often display map-view curvatures ending in horse-tail geometries. Such faults are commonly associated with indentation tectonics, where shortening in front of indenters is transferred laterally to transpression, strike-slip and the formation of transtensional/extensional basins. We investigate how these structurally distinct domains are kinematically linked by the means of a crustal-scale analogue modelling approach where a deformable crust is moved against a stable and rigid indenter. The modelling demonstrates that the geometry of the indenter is the major controlling parameter driving strain partitioning and deformation transfer from thrusting and trans-pression to strike-slip and transtension, whereas the rotation of the mobile plate controls the opening of trian-gular shaped transtensional basins. Flow of the ductile crust leads to the distribution of deformation over a wider area, facilitating strike-slip splaying into transtension/extension behind the indenter. Our results show a very good correlation with the Moesian indentation in the Carpatho-Balkanides system of South-Eastern Europe, where strain is partitioned around the dextral Cerna and Timok strike-slip faults and transferred to thrusting in the Balkanides part of the Moesian indenter and to transtension/extension in the neighbouring South Carpathians.

1. Introduction

Previous studies have shown that strike-slip deformation is often associated with segmentation of fold and thrust belts or mid-ocean ridges, with changes in polarity of subduction systems, as well as with lateral escape of continental lithosphere during indentation (e.g., Mann, 2007 and references therein). These studies have described complex deformation along numerous large-scale continental strike-slip faults, such as the San Andreas Fault (e.g., Anderson 1971.; Wallace, 1990), the Alpine Fault of New Zealand (e.g., Berryman et al., 1992), the North Anatolian Fault (e.g., Aramijo et al., 1999; Neugebauer, 1994), Dead Sea Fault system (e.g., Perinçek and Çemen, 1990; Smit et al., 2008), the Tibetan region and in Indochina (e.g., Chen et al., 2000; Morley, 2013), the Fagnano or the North Scotia Fault of South America (e.g., Lodolo et al., 2003), the Periadriatic Fault of the Alps, or the Mid-Hungarian Fault Zone of the Pannonian basin (e.g., Schmid et al., 2020). Many of

these faults are associated with transpressional orogens or transtensive basins of various geometries and degrees of curvature in map view (e.g., Christie-Blick and Biddle, 1985; Dewey et al., 1998; Smit et al., 2008, 2010, among others). In these settings, the term strain partitioning has often been used in different ways and at different spatial scales to describe the large variability of observed deformation (e.g., Fitch, 1972; Lister and Williams, 1983; Platt, 1993; Carreras et al., 2013). Similar with other studies (Glen, 2004; Cembrano et al., 2005; De Vicente et al., 2009; D'el-Rey Silva et al., 2011; Krézsek et al., 2013; Benesh et al., 2014), we use the term "strain partitioning" to describe a multi-scale distribution of bulk strain into genetically different and coeval struc-tures that cannot be explained by a uniform stress field.

Analogue and numerical modelling studies have demonstrated that the initiation and evolution of strike-slip corridors are always accom-panied with significant strain partitioning, such as between Riedel shears and the main strike-slip fault (e.g. Leever et al., 2011; Dooley and

Schreurs, 2012; Stefanov and Bakeev, 2014; Chemenda et al., 2016; Hatem et al., 2017; Iturrieta et al., 2017; Xiao et al., 2017). This strain partitioning is associated with significant local stress deviations and is more pronounced when either the movement is oblique to the main strike-slip fault, creating restraining and releasing bends with various geometries (e.g., Basile and Brun, 1999; McClay and Bonora, 2001; Smit et al., 2008; Leever et al., 2011; Dooley and Schreurs, 2012; González et al., 2012; Wang et al., 2017; Nabavi et al., 2018), or when the strike-slip fault has a curved geometry (e.g., Smit et al., 2010; Dufréchou et al., 2011). Furthermore, more complex systems of interacting thrusts and strike-slip faults have been observed or modelled (e.g., Duarte et al., 2011; Rosas et al., 2012, 2015; Fedorik et al., 2019). These studies have
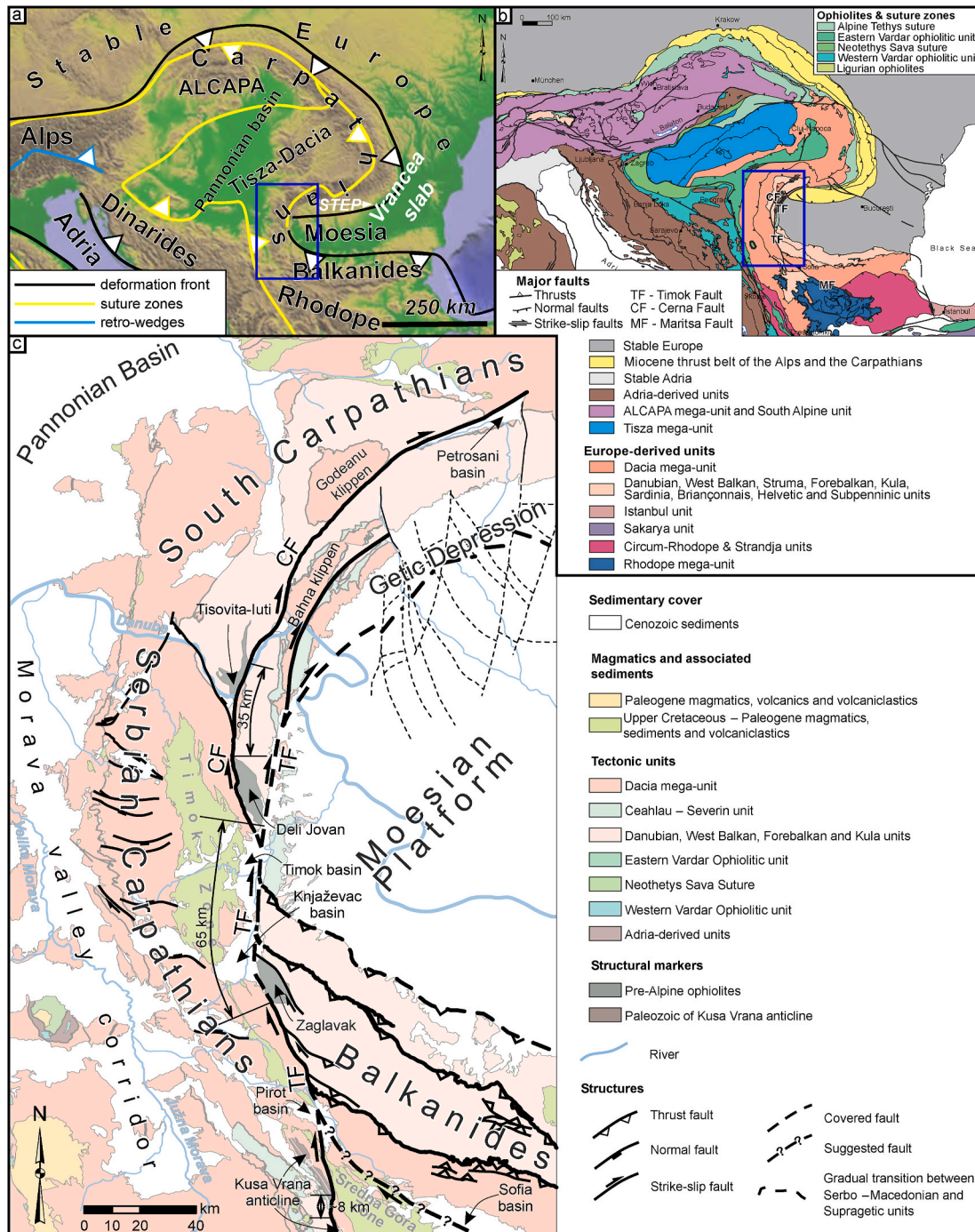
Fig. 1. a) Simplified topographic map of South-Eastern Europe overlain by the first-order structures (orogenic fronts, suture zones and retro-shears) of the Mediterranean Alpine-age orogens (modified from Krstekanić et al., 2020). Blue rectangle shows the location of Fig. 1c. STEP – Subduction-Transform Edge Propagator system in the South Carpathians. White arrow indicates the direction of slab tearing. b) Regional tectonic map of the south-east Europe (simplified after Schmid et al., 2020). Blue rectangle shows the location of Fig. 1c. c) Tectonic map of the Cerna-Timok fault system in the South Carpathians-Serbian Carpathians-Balkanides orocline around the Moesian Platform. Black lines are faults that accommodate deformation related to oroclinal bending. CF – Cerna Fault; TF - Timok Fault. Map is compiled and modified after geological maps of Serbia, Romania and Bulgaria and Maţenco (2017). Structural pattern is modified after Maţenco (2017) and Krstekanić et al. (2020) while the suggested continuation of Timok Fault below the Sofia basin is according to Schmid et al. (2020). (For interpretation of the references to colour in this figure legend, the reader is referred to the Web version of this article.)

also shown that strain partitioning creates a gradual transfer of deformation from contraction to transpression and strike-slip. Other experimental studies have focused on deformation in front of an indenter (e.g., Marshak, 1988; Marshak et al., 1992; Zweigel, 1998 and references therein), where strike-slip deformation accommodates lateral extrusion (Tapponnier et al., 1982; Ratschbacher et al., 1991a, b; van Gelder et al., 2017). Often, strike-slip deformation links shortening in front of the indenter with deformation in another subduction system, such as observed in the Dinarides orogen connecting the shortening in the Alps with Aegean subduction (van Unen et al., 2019), or the Sagaing Fault linking the shortening in the Himalayas with the Sunda subduction zone (e.g., Tapponnier et al., 1986; Morley, 2002; Sternai et al., 2016). In such settings, the geometry and motion of the indenter influences significantly the deformation and structural response around the rigid indenter (Luth et al., 2013). However, the structural link (i.e., kinematics and geometry of major structures) between frontal, usually contractional, and lateral strike-slip deformation around the corner of an indenter is still not well understood.

One of the best examples of strain partitioning along curved strike-slip faults is the one of the Oligocene – middle Miocene Cerna-Timok fault system of the Carpatho-Balkanides orogen in South-Eastern Europe (Fig. 1). Previous studies have shown that this system has cumulated 100 km of dextral offset and links the deformation observed around the Moesian Platform (i.e., a rigid promontory in the prolongation of the East European Craton) along a 180° backarc-convex orocline connecting the South Carpathians, Serbian Carpathians and Balkanides (Fig. 1, e.g., Kräutner and Krstić, 2003; Schmid et al., 2020, and references therein). These studies have also shown that the same system transfers strike-slip deformation to thrusting and extension with variable offsets along its strike.

We aim to advance our understanding of the major parameters controlling strain partitioning and deformation transfer around indenters, with particular application to the Cerna-Timok fault system and associated deformation. To this aim, we performed a series of analogue experiments designed to analyse the deformational response to the shape of the rigid indenter (rounded or rectangular corners), the displacement (translation followed by rotation) along the margins of a rigid indenter and the rheological stratification of the deformable area. With respect to the latter, we analysed the influence of the flow in the ductile crust on the transfer and distribution of deformation. We use image correlation techniques for the detailed analysis of deformation around indenter corners in various experimental setups in order to qualitatively and quantitatively characterize the influence of their geometries on the deformation transfer. We compare the modelling results with the Cerna-Timok fault system of the Carpatho-Balkanides, which allows a detailed understanding of strain partitioning mechanisms during its Oligocene – middle Miocene evolution. We have chosen a strategy in the presentation of our results that involves first the description of a reference model with a simple analogue modelling setup, followed by a parametrical study of other models with a more complex initial geometry or composition. In a separate section we show the relevance of a chosen best-fit model for understanding the evolution of the Cerna-Timok faults system and the associated Carpatho-Balkanides oroclinal bending. All modelling results are subsequently discussed in a process-oriented context.

2. The Cerna-Timok fault system of the Carpatho-Balkanides orogen

The European area connecting the Carpathians and Balkanides orogenic system (Fig. 1a and b) shows a thick-skinned nappe-stack that was formed during two phases of Cretaceous shortening related to the closure of the Ceahlău-Severin branch of the Alpine Tethys Ocean and the subsequent collision between the Dacia mega-unit and the Moesian promontory of the stable European foreland (Săndulescu, 1988; Bojar et al., 1998; Csontos and Vörös, 2004; Iancu et al., 2005; Schmid et al.,

2008, 2020; Maţenco, 2017). The present-day geometry of the orogenic system shows two 180° curved loops, one in the north and east, and another in the south (Fig. 1a). This geometry was ultimately established during the Miocene slab retreat and gradual closure of the Carpathians embayment, consisting of oceanic crust and the continental passive margin of the Alpine Tethys Ocean (Fig. 1b, e g., Csontos and Vörös, 2004; Fügenschuh and Schmid, 2005). The southern 180° arc connects the South Carpathians, the Serbian Carpathians and the Balkanides by creating an orocline with a back-arc convex geometry bent around the Moesian Platform (Fig. 1a and b). The oroclinal bending formed by gradual clockwise rotation and N- to E-ward translation of the Dacia mega-unit during its movement into the Carpathians embayment. The post-Cretaceous rotation was significant (up to 90°) in the South Carpathians when compared to no significant rotation in the Balkanides (e. g., Balla, 1987; Pătraşcu et al., 1994; Márton, 2000; Ustaszewski et al., 2008; van Hinsbergen et al., 2008; Panaiotu and Panaiotu, 2010).

Previous studies have demonstrated that the clockwise rotation was first accommodated by Paleocene – Eocene orogen-parallel extension in the South Carpathians (Matenco and Schmid, 1999; Fügenschuh and Schmid, 2005; Schmid et al., 1998) and subsequently by the evolution of the late Oligocene – middle Miocene curved dextral Cerna and Timok faults system (Fig. 1c, Berza and Drăganescu, 1988; Ratschbacher et al., 1993; Kräutner and Krstić, 2002). Tectonic and lithological markers show that the Cerna Fault (CF) accommodates up to 35 km of dextral offset, as documented by the distance observed between the Godeanu and Bahna klippen, or between the Tisovita-Iuti and Deli Jovan ophiolites (Fig. 1c, Kräutner and Krstić, 2003). In comparison, the Timok Fault (TF) has up to 65 km dextral offset, inferred by the distance observed between the Deli Jovan and Zaglavak ophiolites (Fig. 1c, Kräutner and Krstić, 2003). These faults and their associated structures create a complex deformation system that was inferred to connect the strike-slip, thrusting and extensional deformation around the western margin of Moesia from the Balkanides to the South Carpathians via the Serbian Carpathians (Fig. 1c, Schmid et al., 2020).

One interesting feature of the Cerna – Timok faults system is the formation of Oligocene – Miocene sedimentary basins observed along their strike, such as the Oligocene Petroşani, or the Miocene Timok - Knjaževac basins system (Fig. 1c). These triangular basins are syn-kinematic with respect to strike-slip deformation and formed during the gradual indentation and rotation around the Moesian indenter (e.g., Ratschbacher et al., 1993; Kräutner and Krstic, 2002; Schmid et al., 2020). The Timok - Knjaževac basins system reaches ~17 km in width southwards and is ~98 km in length. To the north, the Timok Fault connects with the late Oligocene - early Miocene transtensional opening of the South Carpathians foredeep (Fig. 1c, the Getic Depression of Răbăgia et al., 2011; Krezsek et al., 2013).

3. Methodology

3.1. Modelling approach

We present a series of 12 crustal scale analogue experiments that portray deformation of the upper to middle crust around a rigid indenter as a consequence of translation and rotation of the material surrounding it. Compared to previous indentation experiments where a rigid indenter is pushed into the model layers (e.g., Tapponnier et al., 1982; Davy and Cobbold, 1988; Ratschbacher et al., 1991a; Luth et al., 2013), our approach has a changed reference frame where the indenter is fixed, while the deformable material moves around it. As such, it allows direct investigation of the variability of deformation styles as a function of position relative to a fixed indenter (i.e., shortening dominated structures orthogonal to the indenter margin and strike-slip dominated structures parallel to the indenter margin) and, in technical sense, provides more flexibility for implementing kinematic boundary conditions (see below) that are relevant for the comparison of modelling results with the natural case, the Carpatho-Balkanides (Fig. 1). Against the

background of the natural example, the key parameters of this study include the shape of the indenter, the rheological stratification of the model crust and the addition of a rotational component of deformation to account for clockwise rotations of 5–10° in Oligocene-Miocene times (Marović et al., 2002).

3.2. Kinematic and geometric setup of the analogue models

All models contain a fixed rigid block, the indenter, with the upper width of 26 cm (Fig. 2a and b), which is scaled to the size (in the N–S direction) of the Moesian Platform in nature (Fig. 1). The indenter is surrounded by deformable layer(s) of brittle or brittle-viscous materials representing the upper to middle crust (Fig. 2). For the description of the modelling setup as well as the modelling results, a relative geographic reference frame with the north oriented upwards is adopted (Fig. 2).

The model indenter is represented by a 2 cm thick stiff polyvinyl chloride (PVC) plate and has either rounded corners (Fig. 2a), or a rectangular geometry (Fig. 2b). The margins of either block have an inclination of 35° dipping towards the surrounding deformable region (Fig. 2d). This inclination approximates the structure at the base of the Cretaceous nappes thrusted over the Moesian promontory (Fig. 1c); Maţenco (2017) and references therein), representing an inherited

feature in the model.

The deformable part of the model is underlain by two basal plastic plates/sheets (Fig. 2). The first, 1 mm thick plastic plate (green in Fig. 2), underlies the entire model (including the rigid block), is mobile and is attached to a motor (through a bar that is connected to the model and motor by mechanical joints). The motor pulls it northward with a constant velocity of 10 cm/h or 2 cm/h for brittle only or brittle-viscous models, respectively. Depending on the specific model boundary conditions, this plastic plate is either only translated or translated and rotated. The rotation is achieved around a pole of rotation represented by a stationary pin protruding from below the indenter (fixed pin in Fig. 2). In our experiments, the fixed pin is located at the northern end of the straight segment of rounded indenter's western margin or at the north-western corner of the rectangular shaped indenter (Fig. 2a–c). The mobile plastic plate has a cut in the middle in the north-south direction (dashed green line in Fig. 2) to enable the sliding and rotation of the mobile plate along a stationary pin (Fig. 2). This construction allows for a combined translational-rotational movement of the mobile plate. The second, 0.1 mm thick plastic sheet (grey in Fig. 2), is fixed and overlies the moving plate north of the rigid block, while underlying this moving plate to the north-west. This change takes place at the cut in the moving plate. We have chosen this configuration to prevent deformation north
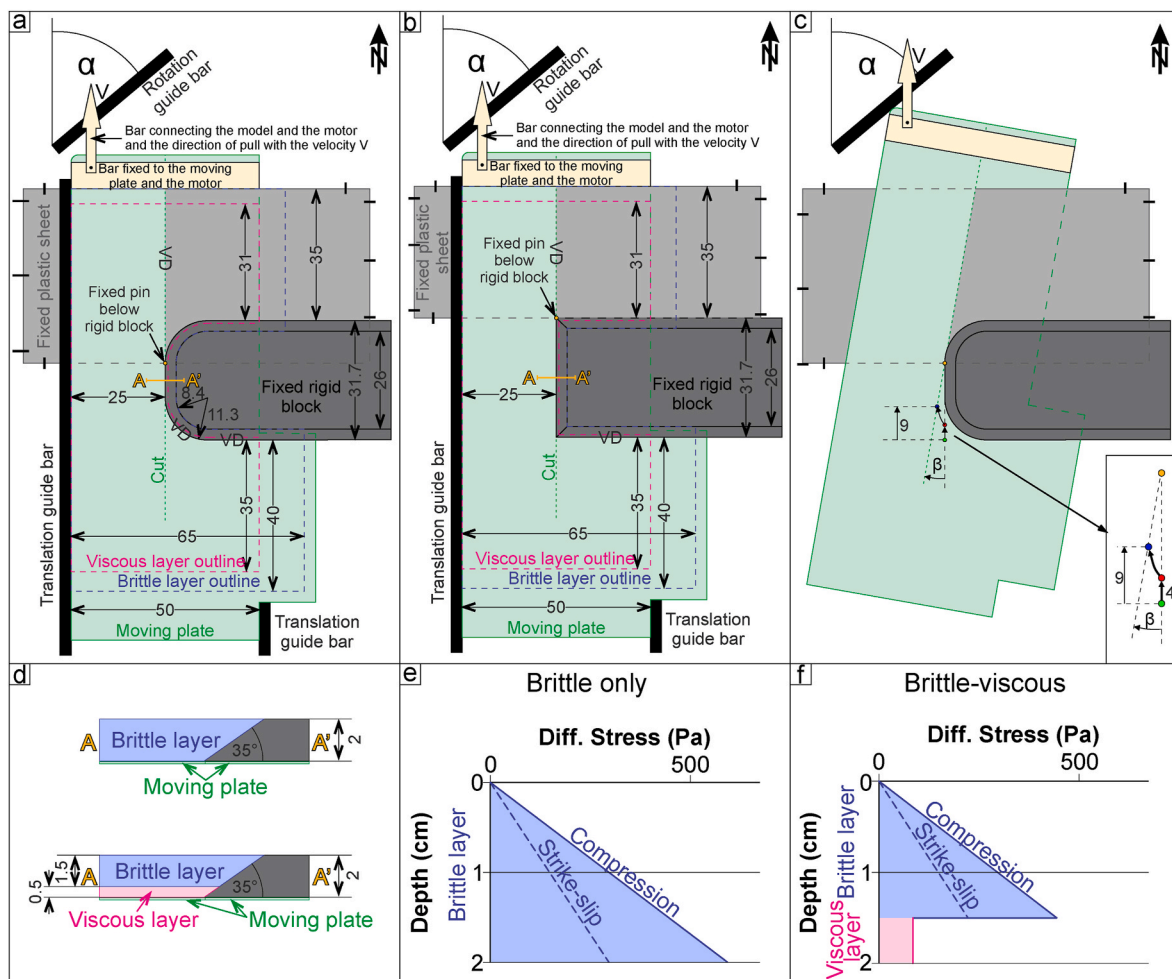
Fig. 2. Modelling setups. Adopted orientation is geographical with up being relative north. All numbers in Fig. 2a–d are in centimetres. a) Initial setup of experiments with rounded indenter's corners. b) Initial setup of experiments with rectangular indenter's corners. c) Configuration at the end of the experiment in Fig. 2a. Inset: Movements of the moving plate include the first phase of 4 cm of translation (green to red circle) and the second phase of combined translation/rotation kinematics (red to blue circle) that results in a total of 9 cm of northward translation and a final clockwise rotation angle β around the pole (yellow circle). In Fig. 2a–c the angle of the fixed rotation guide bar α equals to 0°, 30° and 50°, which corresponds to an induced rotation angle β of 0° (no rotation), 5° and 10° respectively. d) Setup cross-sections for brittle-only and brittle-viscous experiments in Fig. 2a and b. e) Strength profile for brittle-only experiments. f) Strength profile for brittle-viscous experiments. (For interpretation of the references to colour in this figure legend, the reader is referred to the Web version of this article.)

of the rigid block, where, otherwise, extension along the northern edge of the indenter would take place. At the same time, the area to the north-west of the rigid block is free to move. This setup predefines velocity discontinuities (VD) along the southern and western margins of the rigid block and along the contact between the moving plate and fixed plastic sheet (Fig. 2a–c). All experiments are confined laterally by either guiding bars or sand (Fig. 2a and b), which in the case of brittle-viscous experiments prevent the viscous layer to induce boundary effects by lateral flow outside the model area.

In experiments with no rotation (Table 1), the northward displacement of the mobile plate is 9 cm. For experiments with rotation (Table 1), we apply a stepwise approach by following previous experimental studies (Farangitakis et al., 2019, 2021). An initial 4 cm of northward translation is followed by a phase of combined translation and rotation. The purpose of these two phases of imposed kinematics is to create strike-slip deformation (in the first phase) and to study influence of coupled rotation and translation (the second-phase) on the pre-existing strike-slip faults. This complex movement of the mobile plate is guided by a fixed bar located in the north (Fig. 2a–c). During the experiment, when the mobile plate hits the rotation guide bar, we remove the lateral translation guide bars to enable the combined rotational and translational movement (Fig. 2c). The total clockwise rotation reaches 5° and 10° in different models (Table 1). Similar to experiments with no rotation, the total northward displacement of the moving plate along the western margin of the rigid block is 9 cm (Fig. 2c).

The experiments presented in this study are subdivided in two groups. Group 1 (models 1–6) consists of experiments with rounded indenters whereas group 2 experiments (models 7–12) are characterized by rectangular indenters (Table 1). These distinct indenter geometries allow to quantitatively and qualitatively compare effects of corner geometry in cases where deformation is gradually transferred (rounded corners) and where the deformation transfer is more abrupt (90° corners). For each of these groups we performed experiments with and without a rotational component applied to the deformable area surrounding the indenter as well as of brittle and brittle-viscous composition, respectively.

3.3. Model materials and scaling

In our models, the brittle layer consists of dry quartz sand with a bulk density of ρ = 1500 kg/m³, a cohesion of 10–40 Pa and coefficients of friction of 0.63, 0.48 and 0.52, representing peak, dynamic and reactivation friction, respectively (Willingshofer et al., 2018). The sand has a grain-size spread of 100–300 μm and exhibits Mohr-Coulomb behaviour, which makes it a suitable analogue for natural brittle upper crust (Krantz, 1991; Dooley and Schreurs, 2012; Klinkmüller et al., 2016; Schellart and Strak, 2016). Thin marker horizons of coloured quartz sand were used as passive markers to show vertical offsets along faults in cross-sections, while horizontal offsets are tracked by passive maker lines of black and yellow quartz sand placed on the model upper surface.

The viscous layer in brittle-viscous models is the analogue of the ductile crust below the brittle-ductile transition. It consists of poly-dimethylsiloxane (PDMS silicon polymer) putty, mixed with iron powder and quartz sand as fillers in order to increase the density of pure PDMS (i.e., 970 kg/m³) to a value close to the bulk density of overlying quartz sand layer. This viscous mixture has a density of ρ = 1470 kg/m³ and viscosity of $3.8 \cdot 10^4$ Pas at room temperature. The viscosity of the viscous mixture has been determined with a coni-cylindrical viscometer. An n-value of 1.2 indicates slightly non-Newtonian behavior. We assume that for low stresses and low strain rates (i.e., similar to those used in analogue models) behavior of the viscous mixture is essentially Newtonian (e.g., Broerse et al., 2019; Rudolf et al., 2016; Weijermars and Schmeling, 1986).

Scaling of all models follows the principles of geometrical, rheological and kinematical similarities between natural systems and models (Hubbert, 1937; Ramberg, 1981; Weijermars and Schmeling, 1986; Davy and Cobbold, 1991). Densities of our material of 1500 kg/m³ represent natural upper to middle crust densities of 2750 kg/m³, yielding a density-scale ratio ρ* (ρ_{model}/ρ_{nature}) of 0.55. The length scale in our experiments is such that 1 cm in model corresponds to 7 km in nature, yielding a length-scale ratio L* (L_{model}/L_{nature}) of $1.43 \cdot 10^{-6}$. We choose the length scale ratio such that the brittle-viscous transition in the models is at a depth of ca. 10 km when scaled to nature. This depth of the brittle-viscous transition is consistent with a change in deformation behavior of quartz-dominated lithologies from frictional sliding to creep (e.g., Kerrich et al., 1997; van der Pluijm and Marshak, 2004) for average continental geo-thermal gradients in the order of 30 °C/km (Turcotte and Schubert; 2014; Limberger et al., 2014, 2018) and the depth extent of weak seismicity documented in the South- and Serbian Carpathians (e.g., Dimitrijevic, 1994; Popa et al., 2018). At this depth the vertical stress (i.e., lithostatic stress, σ = ρ·g·h, where ρ is quartz sand density, g is gravitational acceleration and h is the thickness of overlying sand layer) in the experiments is 220 Pa, corresponding to 280 MPa in nature, which results in a stress-scale ratio of $7.87 \cdot 10^{-7}$. Strength profiles (Fig. 2e and f) are representative for the initial conditions and have been calculated following Brun (2002). To scale model velocity in brittle-viscous models, we use a time-scale ratio t* = $5.3 \cdot 10^{-11}$ calculated as (Hubbert, 1937):

$$t^* = \frac{1}{\dot{\gamma}^*} \tag{1}$$

while shear strain rate ratio $\dot{\gamma}^*$ equals:

$$\dot{\gamma}^* = \frac{V^*}{L^*} \tag{2}$$

where velocity ratio V* = $2.7 \cdot 10^4$ means that 2 cm/h in models scales to 0.65 cm/yr in nature, which is consistent with the 60–65 km displacement along the Timok fault over a period of ca. 10 Myr (e.g., Kräutner and Krstić, 2003; Schmid et al., 2020). Note that the shear strain rate is

Table 1
Model parameters. Model type: b - brittle only, b-v– brittle-viscous.

Model number	Model type	Brittle layer thickness (cm)	Viscous layer thickness (cm)	Rigid block geometry	Engine pull velocity (cm/h)	Total translation (cm)	Total CW rotation (°)	Scaled thickness (km)
1	b	2	–	Rounded corners	10	9	0	14
2	b	2	–	Rounded corners	10	9	5	14
3	b	2	–	Rounded corners	10	9	10	14
4	b-v	1.5	0.5	Rounded corners	2	9	0	14
5	b-v	1.5	0.5	Rounded corners	2	9	5	14
6	b-v	1.5	0.5	Rounded corners	2	9	10	14
7	b	2	–	90° corners	10	9	0	14
8	b	2	–	90° corners	10	9	5	14
9	b	2	–	90° corners	10	9	10	14
10	b-v	1.5	0.5	90° corners	2	9	0	14
11	b-v	1.5	0.5	90° corners	2	9	5	14
12	b-v	1.5	0.5	90° corners	2	9	10	14

calculated as velocity over the thickness of the viscous layer. For the calculated experimental velocities, the viscosity of the modelling material scales to natural viscosities of $\sim 10^{21}$ Pas, which is in the range of quartz dominated ductile crust below the brittle-ductile transition (e.g. Hirth et al., 2001).

3.4. Experimental procedures, recordings and PIV-derived strain analysis

Models are built and run in a normal gravity field and at room temperature (i.e., 19–20 °C). An electric motor imposes a constant velocity on the mobile plastic sheet. Depressions deeper than 1 mm are filled manually, using a funnel, with alternating layers of differently coloured sand, representing syn-kinematic sedimentation. At the end of each experiment, two post-kinematic layers of black and white sand are added on top of the entire model to preserve topography and water is sprinkled on the sand layers to increase cohesion within the sand and to allow for sectioning of the experiments to obtain information on the internal structures.

We monitor surface deformation by taking top-view photographs (by using Panasonic Lumix DC-G9 with 20.3 megapixels for models 1–6 and 10–12 and Canon EOS 700D with 18.0 Megapixels for models 7–9) at regular time intervals of 45 s for brittle only experiments, and 3 min for brittle-viscous models, corresponding to 0.125 cm and 0.1 cm of translation displacement between two photographs, respectively. These top-view photographs are analysed using image correlation techniques (PIVlab, Thielicke and Stamhuis, 2014) in order to calculate incremental particle displacements. Subsequently, we remove very large displacements due to incorrect correlations by applying a magnitude threshold filter, followed by a visual inspection for remaining outliers and their manual removal and interpolation of displacements in basin areas for time frames when sedimentation is applied (i.e., only for few time frames in a model). Displacements for these time frames are interpolated taking displacement values on the margin of basins unaffected by sedimentation. The image correlation provides the displacement fields in a fixed spatial reference frame. However, model materials show large motions through this spatial frame. We therefore also track material by defining an initial regular grid that deforms at each time step using the interpolated, spatial displacement fields (i.e., Lagrangian summation, similar to Senatore et al., 2013; Stanier et al., 2016; Boutelier et al., 2019; Krýza et al., 2019). From the material displacements the incremental deformation field is calculated (Supplementary Appendix A, D). As the deformation is large, small strain definitions are no longer valid (Malvern, 1969). Therefore, we describe the finite deformation as a product of the stretch tensor (corresponding to the shape change), and a rotation tensor, using a polar decomposition of the finite deformation gradient tensor (Broerse et al., 2021). Note that the principal stretches (λ_i) relate to principal strains (ε_i) as: $\lambda_i = 1 + \varepsilon_i$.

For small, incremental strains one can use the ratio of the largest to the smallest principal strain to determine a strain type in the horizontal plane: extension, strike-slip, shortening and their transitions (Kreemer et al., 2014). From Broerse et al. (2021) it follows that, for the mentioned types of strain, the logarithms of principal stretches for large deformation have the same ratios as incremental small strains. Therefore, we use the logarithmic principal stretches to determine the average strain type during model evolution (see Supplementary Appendix B, E; see also Broerse et al., 2021). While in 3D, faulting always involves shear on fault planes, in horizontal view only strike-slip faulting is a purely shear; thrust faulting will appear as shortening in 2D, while normal faults appear as extensional features. Our approach relies on the assumption that the surface deformation is not affected by subsequent phases of opposite deformation. If inversion of deformation occurs, the analysis should be divided in separate periods. Finally, these results are combined with visual interpretations of cross-sections to infer 2D strain in the entire, 3D model.

3.5. Experimental limitations and simplification

The analogue models presented in this study do not account for isostasy, temperature gradients with depth (i.e., viscosity of the viscous layer is constant, which is an acceptable approximation following Davy and Cobbold, 1991), surface erosion and sediment transport. Therefore, topographic heights are exaggerated in the contractional area in front of the indenter. Despite these limitations, we are confident that the modelling results are meaningful, because we mostly focus on the area of the model where significant deformation is by strike-slip, which generally produces little thermal perturbations as well as low topography changes. Le Guerroué and Cobbold (2006) demonstrated that syn-kinematic erosion and/or sedimentation in a strike-slip setting only have minor effects on structural patterns, yet the results have been obtained at higher spatial resolution. As such, minor differences in structural patterns within strike-slip zones with or without syn-kinematic sedimentation are not significant on the scale of our models. Therefore, surface processes are in our view not among the controlling factors during the oroclinal bending of the Carpatho-Balkanides.

Compared to the natural case of the Serbian Carpathians and its Cretaceous inherited structures (Fig. 1c), our models do not have inherited topography and/or a wedge structure (i.e., and inherited mountainous fold and thrust belt) in the deformable part of the model prior to deformation. This simplification is justified because the Cerna-Timok fault system offsets the inherited Cretaceous nappe stack and Paleocene-Eocene Danubian extensional dome in the Serbian and South Carpathians (e.g., Kräutner and Krstić, 2003; Fügenschuh and Schmid, 2005) and do not represent reactivated nappe contacts. Such simplification allows studying first-order structural responses to the varied parameters without complex overprinting interactions with earlier deformation.

## 4. The reference model and parametrical study

The results are described starting with a detailed analysis of a "reference model" (Model 1, Fig. 3), to which we compare the results of a parametric study (Figs. 4–7) and the best-fit model (Fig. 8). The latter serves to demonstrate the relevance of the modelling results for the evolution of the Cerna-Timok fault system and the associated Carpatho-Balkanides oroclinal bending. Note that the transpressional deformation in the northernmost segment of all models (i.e., at larger distances from the pole of rotation), results from the modelling setup (N–S oriented velocity discontinuity, Fig. 5) and is not relevant for the comparison with the natural case of the Carpatho-Balkanides.

Modelling results are described based on the structural interpretation of top-view photographs and cross-sections and results of digital image correlation methods documenting the variability of strain regimes in map-view (Figs. 3–5 and 8). Furthermore, we use time-lapse top-view videos of incremental strain components and cumulative strain type, available in the Supplementary Appendix A, B, D, E and temporal evolution of selected grid cells (Supplementary Appendix C and F) to derive and explain detailed fault kinematics and their interplay during deformation.

4.1. Reference model: model 1

Model 1 consists of a rigid indenter with rounded corners, while the surrounding, deformable material is entirely brittle (Table 1, Fig. 2a, e). Deformation results only from northward translation of the model layers.

Model 1 (Fig. 3) documents the development of distinct strain regimes in time, which are characterized by predominantly strike-slip deformation along the N–S oriented flank of the indenter, transpression along the curved indenter segment and contraction at the E-W striking margin of the indenter. The partitioning into these deformation regimes takes place during the entire experiment, although structural
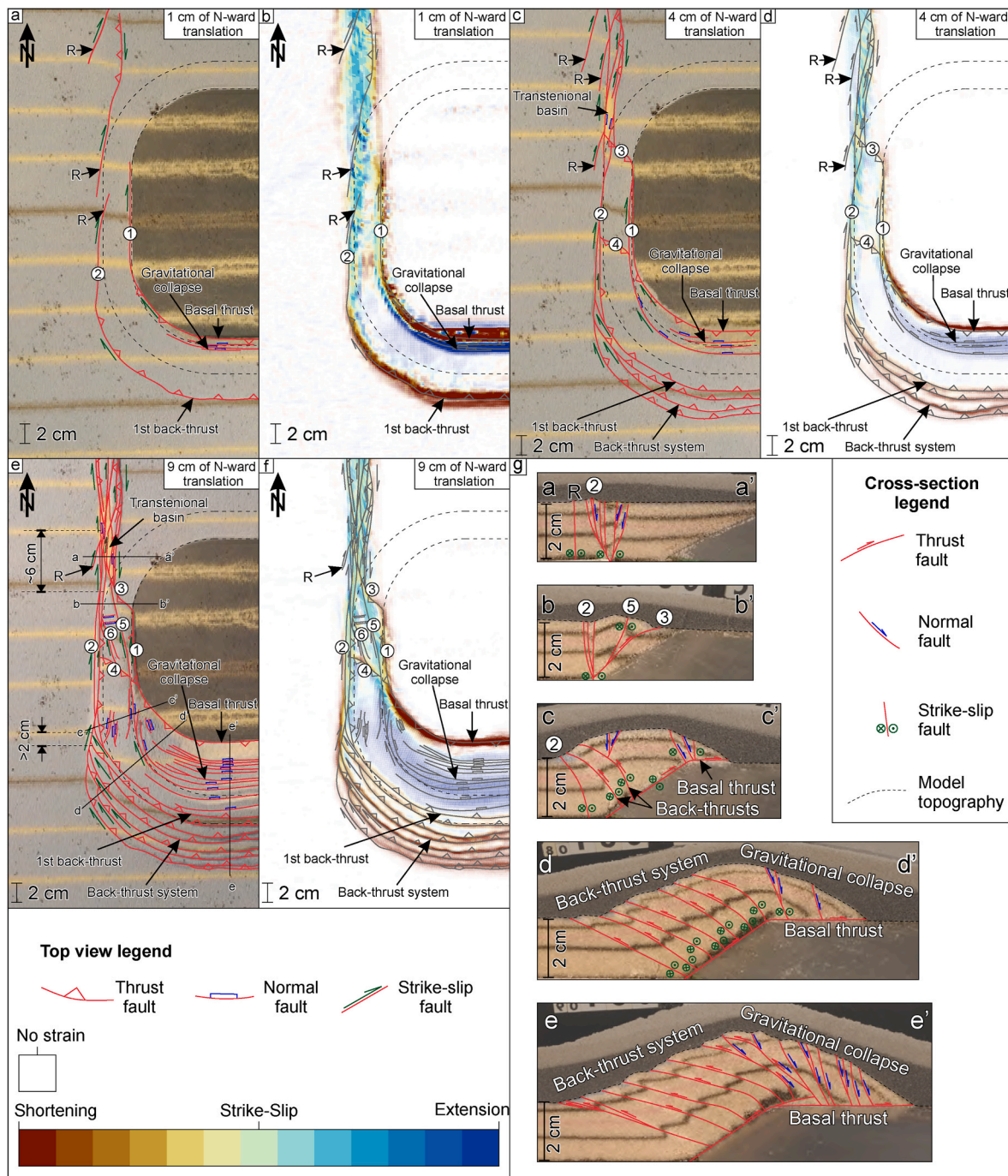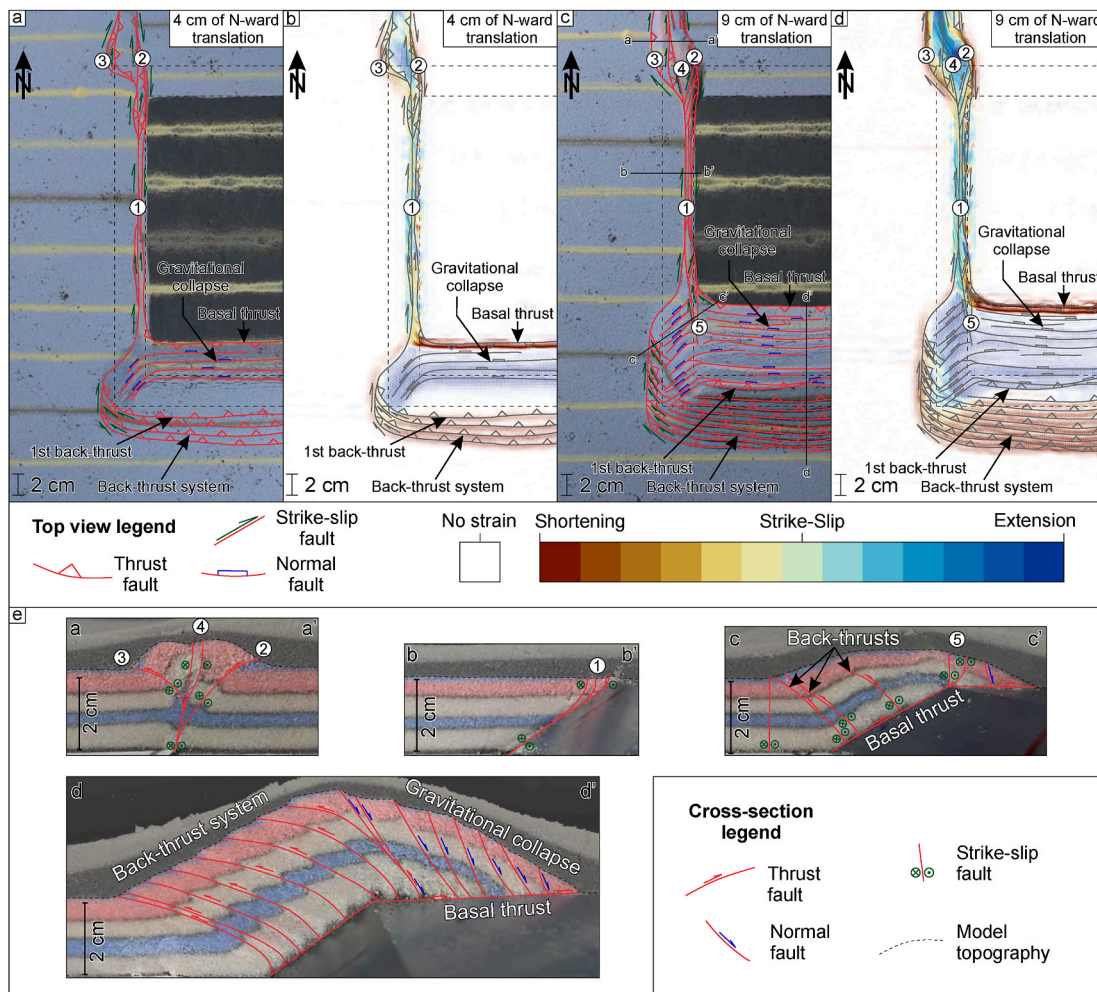
Fig. 3. Model 1 - reference model. Dashed black lines mark the upper and lower edges of the indenter. R – Riedel shear. a) Interpreted top-view photo after 1 cm of northward translation. b) Cumulative strain type map after 1 cm of northward translation. To supress areas without significant deformation, the transparency of areas with a strain magnitude below the 95 percentile is increased. We define the strain magnitude as the maximum, absolute logarithmic principal stretch (i.e. maximum absolute Hencky strains). c) Interpreted top-view photo after 4 cm of northward translation. d) Cumulative strain type map after 4 cm of northward translation. e) Interpreted top-view photo at the end of the experiment. f) Cumulative strain type map at the end of the experiment. Strain plots in Fig. 3b, d and f are overlain with visually interpreted structures from Fig. 3a, c and e (grey lines). Strain colour legend corresponds to Fig. 3b, d and f. g) Cross-sections of the reference model at the end of the experiment. Dashed line marks the model topography at the end of the experiment. Shaded area in the upper part of each cross-section marks post-kinematic sand cover. Cross-section locations are shown in Fig. 3e. (For interpretation of the references to colour in this figure legend, the reader is referred to the Web version of this article.)

complexity increases through time (Fig. 3; see also Supplementary Appendix A and B that show the incremental 2D strain with time and the evolution of average strain type).

4.1.1. Early stages

In the early stages of the experiment, deformation is localized along the western and southern margins of the indenter (Fig. 3a and b). In particular, strike-slip deformation localized along the western indenter margin interface, while being distributed above the VD (see Supplementary Appendix A, B). This suggests that lower vertical stress levels above the ramp facilitate the onset of deformation at this location (structure 1 in Fig. 3a). However, a new strike-slip fault zone forms

Fig. 4. Model 7 – brittle only model with rectangular indenter and no rotation. Dashed black lines mark the upper and lower edges of the indenter. a) Interpreted top-view photo after 4 cm of northward translation. b) Cumulative strain type map after 4 cm of northward translation. To supress areas without significant deformation, the transparency of areas with a strain magnitude below the 95 percentile is increased. We define the strain magnitude as the maximum, absolute logarithmic principal stretch (i.e., maximum absolute Hencky strains). c) Interpreted top-view photo at the end of the experiment. d) Cumulative strain type map at the end of the experiment. Strain plots in Fig. 4b and d are overlain with visually interpreted structures from Fig. 4a and c (grey lines). Strain colour legend corresponds to Fig. 4b and d. e) Cross-sections of the model 7 at the end of the experiment. Dashed line marks the model topography at the end of the experiment. Shaded area in the upper part of each cross-section marks post-kinematic sand cover. Cross-section locations are shown in Fig. 4c. (For interpretation of the references to colour in this figure legend, the reader is referred to the Web version of this article.)

afterwards (structure 2 in Fig. 3a) above the lower edge of the indenter's inclined margin that coincides with the basal VD. NNE-SSW oriented Riedel shears (R in Fig. 3a) are related to the northward translation of the mobile sheet, suggesting early strain partitioning. As the shear zone in the north evolves, an area of transtensional strain (light blue shades in Fig. 3b), related to dilation during shearing is bounded by areas which underwent slight shortening and transpression (pale red, orange and yellow values in Fig. 3b). This shear zone develops into a positive flower structure in the north, with oblique-slip thrusts bounding the strike-slip corridor (Fig. 3c–f). Along the western margin of the rigid block, the deformation after 1 cm of displacement is mostly accommodated by the two early formed N–S oriented strike-slip faults (1 and 2 in Fig. 3a). In the early stages of deformation, these two faults are connected around the SW corner of the indenter to the E-W oriented shortening domain in the south. This connection is achieved through a basal thrust along the pre-existing indenter ramp and a back-thrusting system where the offset is initiated at the toe of the ramp (Fig. 3a, g). The overall system transfers N–S strike-slip into E-W oriented thrusts and back-thrusts (Fig. 3b).

4.1.2. Formation of the main N–S oriented strike-slip fault

After approximately 4 cm of displacement of the mobile sheet (Fig. 3c and d), all Riedel shears are connected and the main N–S oriented strike-slip fault (structure 2) represents a thoroughgoing strike-slip system. This structure is characterized by a change in fault dip angle, from sub-vertical in the north to steeply eastward-dipping in the south (e.g., compare cross-sections a-a', b-b' and c-c' in Fig. 3g), consistent with a southward increase of the reverse component of movement (Fig. 3g). Overall, the deformation zone gets wider southwards when approaching the rounded corner of the indenter (Fig. 3e), as the cumulated deformation is changing from strike-slip and transtension in the north to strike-slip and transpression in the south (Fig. 3f–g). Furthermore, the final dextral offset along the main strike-slip fault (structure 2) decreases towards south from ~6 cm to <2 cm (see the offset in black and yellow marker lines in top view, Fig. 3e).

The initial strike-slip structure (1 in Fig. 3e and f) and the main strike-slip fault (2 in Fig. 3e and f) are connected by obliquely oriented thrusts in map view (3 and 4 in Fig. 3c–f, cross-section b-b' in Fig. 3g) and NNW-SSE oriented strike-slip faults (5 and 6 in Fig. 3e and f, cross-section b-b' in Fig. 3g). These thrusts develop on top of the inclined margin, adding to the complexity in the strain pattern in the central
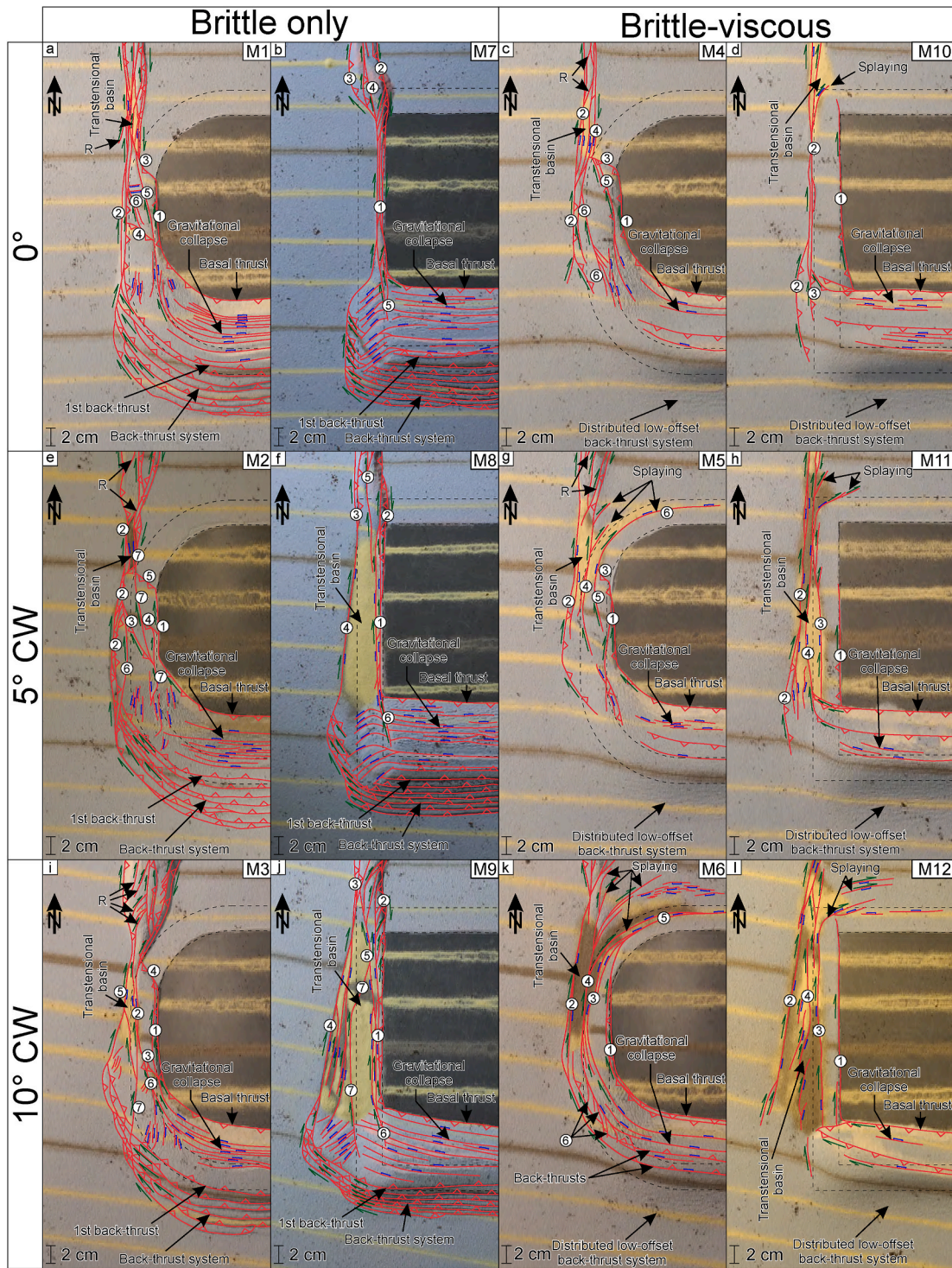
Fig. 5. Interpreted top-view photos taken at the end of all 12 experiments. Numbers indicate sequence of major fault activation in the strike-slip zone. Dashed black lines mark the upper and lower edges of the indenter. Legend is the same as in Fig. 3.

segment of the model (Fig. 3f), where strain is partitioned between top to N shortening (red along 3 and 4 in Fig. 3f), strike-slip (green) and transtension (light blue values) in the centre of the deformation zone (structures 5 and 6 in Fig. 3f), while bounded by transpressional deformation (orange values along 1 and 2 in Fig. 3f).

4.1.3. Transition between strike-slip and thrusting

The SW corner of the rigid block (Fig. 3e and f, cross-section d-d' in Fig. 3g) represents the area where strike-slip deformation transitions to

thrusting with significant changes of fault orientations. The strike of major structures follows the predefined curvature of the rigid block resulting in curved geometries of the back-thrusts and the normal faults. Back-thrusting is transferred directly to the strike-slip deformation, demonstrating oblique dextral reverse slip in the bending zone (Fig. 3a–f). This connection evolves sequentially as the main strike-slip fault propagates farther to the south to connect with newly formed back thrust (see Supplementary Appendix A, B). N-dipping normal faults are linked with the main strike-slip fault (structure 2) through NNW-SSE
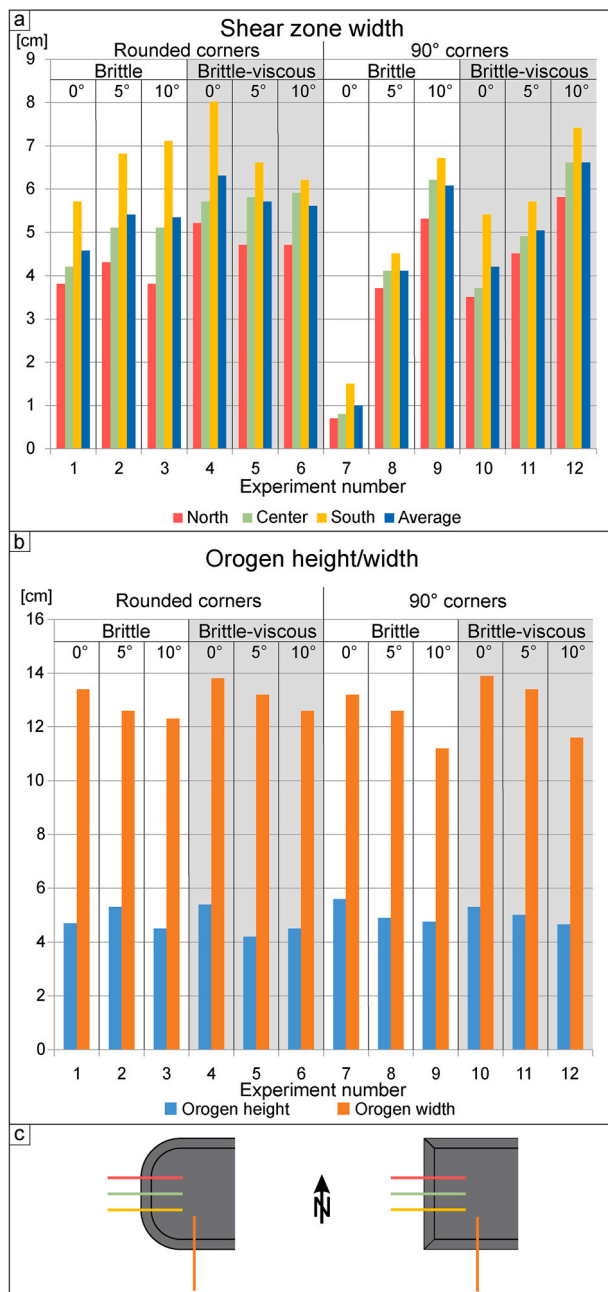
Fig. 6. a) Histogram of the strike-slip zone width perpendicular to the western indenter's margin in each experiment measured in the north, centre and the south of the zone, and their average. All measurements are done visually on the top-view photographs at the end of the experiment. We define the strike-slip zone width as the distance between two bounding faults with a visually observable offset. b) Chart of orogen (thrusting wedge) height and width. Orogen height is measured in cross-sections and orogen width in top-view photographs at the end of the experiment, perpendicular to the southern margin of the indenter. We define the orogen width as the distance between two bounding faults with visually observable offset. c) Top-view locations of the sections along which we determine the strike-slip zone and orogen widths.

oriented dextral faults (5 and 6 in Fig. 3e and f), while the basal thrust remains linked to the oblique strike-slip fault along the western edge of the indenter (1 in Fig. 3e and f). This gradual transfer is further marked by a decrease in contractional or extensional strain, characterizing an area of distributed deformation without clear faulting (decrease in red and blue intensity westward along the basal thrust, in the region of the gravitational collapse and back-thrust system in Fig. 3f). In this area the

strain type changes from shortening and extension in the south (red and blue in Fig. 3f, respectively) to oblique-slip (orange, yellow, light blue values) and strike-slip (green) in the west. This change is associated with a decrease in vertical offset in the back-thrust system from 3.3 cm in the south (cross-section e-e' in Fig. 3g) to 1.9 cm in the SW corner area (cross-section d-d' in Fig. 3f). Minor E− and W- dipping normal faults in the bending region (Fig. 3e–g, cross-sections c-c' and d-d') display very small offsets, accommodating the topographic transition from elevated shortening dominated wedge south of the indenter to strike-slip dominated low-topography structures to the west of the indenter.

Directly south of the indenter, the displacement is perpendicular to the rigid block. In this part of the system, the inclined margin acts as a thrust ramp, along which material has been transported on top of the rigid block, resembling a flat-ramp-flat geometry (Fig. 3g, cross-section e-e') or Coulomb wedge model with fore- and retro-wedges (e.g., Davis et al., 1983; Dahlen et al., 1984; Del Castello et al., 2004). The final strain type map (Fig. 3f) demonstrates that most thrusting deformation is accommodated along the basal thrust (see also cross-sections d-d' and e-e' in Fig. 3g). The S-verging back-thrusts are partly re-activated as N-dipping normal faults to accommodate the change in geometry of the basal thrust from the ramp to the flat segment (Fig. 3e and f, cross-section e-e' in Fig. 3g; see also Supplementary Appendix C).

4.2. Parametrical study

In the following sections we provide a concise overview of modelling results for the parameter space explored in this study. We start with highlighting similarities and differences of modelling results for different indenter geometries (Figs. 3–5) and amount of rotation for set-ups where the crust consists of brittle material only (Fig. 5). Thereafter, we describe the results for models with brittle-ductile rheological stratification, for which we similarly vary the indenter shape and amount of rotation (Fig. 5). Next to displaying the modelling results as interpreted top-view images, cross sections or strain maps (see also M1), histogram diagrams are used for the quantitative analysis of modelling results relating the size (i.e., width, of strike-slip dominated shear zone, width, length and depth of basin, width and height of orogen) of structural features to the tested parameters (Figs. 6 and 7).

4.2.1. The influence of the indenter geometry

Our analysis of models with rounded (M1) and rectangular (M7) indenter corners subject to translational kinematic boundary conditions (Figs. 3, 4 and 5a, b) show that the indenter geometry significantly influences the geometry and kinematics of strike-slip zones and their transition to the E-W oriented thrust systems (compare Fig. 5a and b).

In case of rounded indenter corners the strike-slip system along the western margin is distributed over a wider area compared to models with rectangular corners (Figs. 3 and 4). In particular, the average width of the strike-slip zone is 4.6 cm in M1, while it is 1 cm in M7 (Figs. 5 and 6a). This difference is a consequence of how the strike-slip and thrust domains connect. For rounded indenters it is the first back-thrust of the thrust domain that connects with the major strike-slip fault that develops at the VD along the western indenter margin (Fig. 3a and b), whereas it is the basal fore-thrust that connects with the strike-slip fault along the upper indenter-model boundary in the case of the rectangular indenter (Fig. 4a and b). The latter is probably an effect of stress concentration at indenter corners localizing deformation close to the sand-indenter boundary (Fig. 4). This difference in model evolution has major implications for the style and kinematics of deformation at the transition of the strike-slip to the thrusting domain where M1 shows a gradual change from thrusting to strike-slip deformation (Fig. 3e and f). In contrast, this transition is abrupt in M7 and defined by an array of small dextral faults with an important normal slip component (Fig. 4). These faults link to displacement along the main strike-slip fault zone cutting the evolving thrust wedge (Fig. 4c and d).

These first-order features are also observed when combining
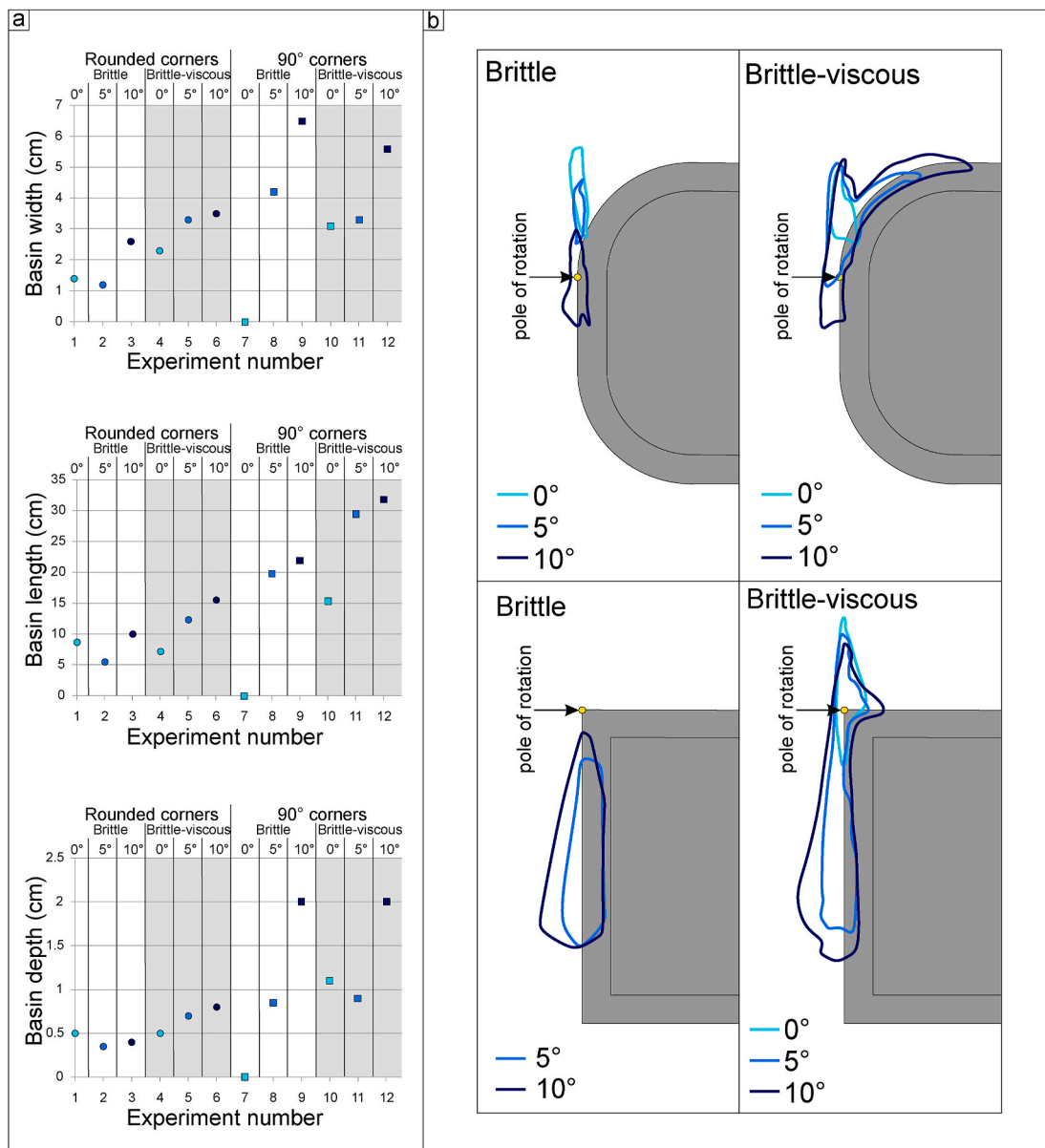
Fig. 7. Basin geometry parameters and top-view shape and position. a) Charts of basin width, length and depth in each experiment. Basins' widths and lengths are measured in the final top-view photos in the E-W and N–S direction. Basin depths are obtained from the cross-sections. b) Top-view basin location and geometry at the end of each experiment relative to the indenter, taken as the outline of the syn-kinematic sediments in the final top-view photograph.

translation with rotation of the moving sheet (Fig. 5 e, f, i, j) and are less pronounced when adding a viscous layer at the bottom of the models (Fig. 5c, d, g, h, k, l).

*4.2.2. The influence of imposed rotation*

Including rotation leads to a systematic widening of the deformed area, particularly of the strike-slip dominated domain (Fig. 5). This effect is more pronounced when indenter corners are rectangular. For example, when comparing models with rectangular corners (Fig. 5b, f, j), the average strike-slip zone width in models with no rotation is as low as 1 cm (model 7), ~4 cm for 5° of rotation (M8) and ~6 cm for models with 10° rotation (M9; Fig. 6a). These differences are related to the scissor-style opening of, in map-view, triangular-shaped transtensional basins above the basal velocity discontinuity (Figs. 5 and 7). As such these basins are narrower and shallower in the north but wider and deeper in the south where the extensional component is largest (M8 and M9, Figs. 6 and 7). Progressive rotation also induces the formation of new strike-slip faults with normal component of slip (e.g., fault 7 in

Fig. 5j) within the evolving sedimentary basin, which cut into the orogenic wedge at the transition zone. Furthermore, the orogenic wedge gets lower and less wide with increasing amount of rotation for both, models with rounded and rectangular indenter corners (Fig. 6b).

Models with curved indenter also show widening of the deformation zone away from the rotation pole, which is, however, less pronounced compared to models with rectangular corners (compare M2 and M3 with M8 and M9, Fig. 5). Consequently, these transtensional basins are smaller and less deep (width: 1.2–2.6 cm, length: 5.0–10.0 cm, depth: 0.3–0.4 cm; Fig. 7). Similar to models with rectangular corners, widening of the strike-slip deformation zone is also associated with the formation of new faults that link this zone to the thrust wedge (e.g., fault 4 in Fig. 5k).

4.2.3. The influence of rheology: brittle-only vs. brittle-viscous rheology

In models with a viscous layer, deformation is distributed over a wider area but a smaller number of discrete structures is formed that accommodate the motion of the underlying plate (Figs. 5 and 6). The
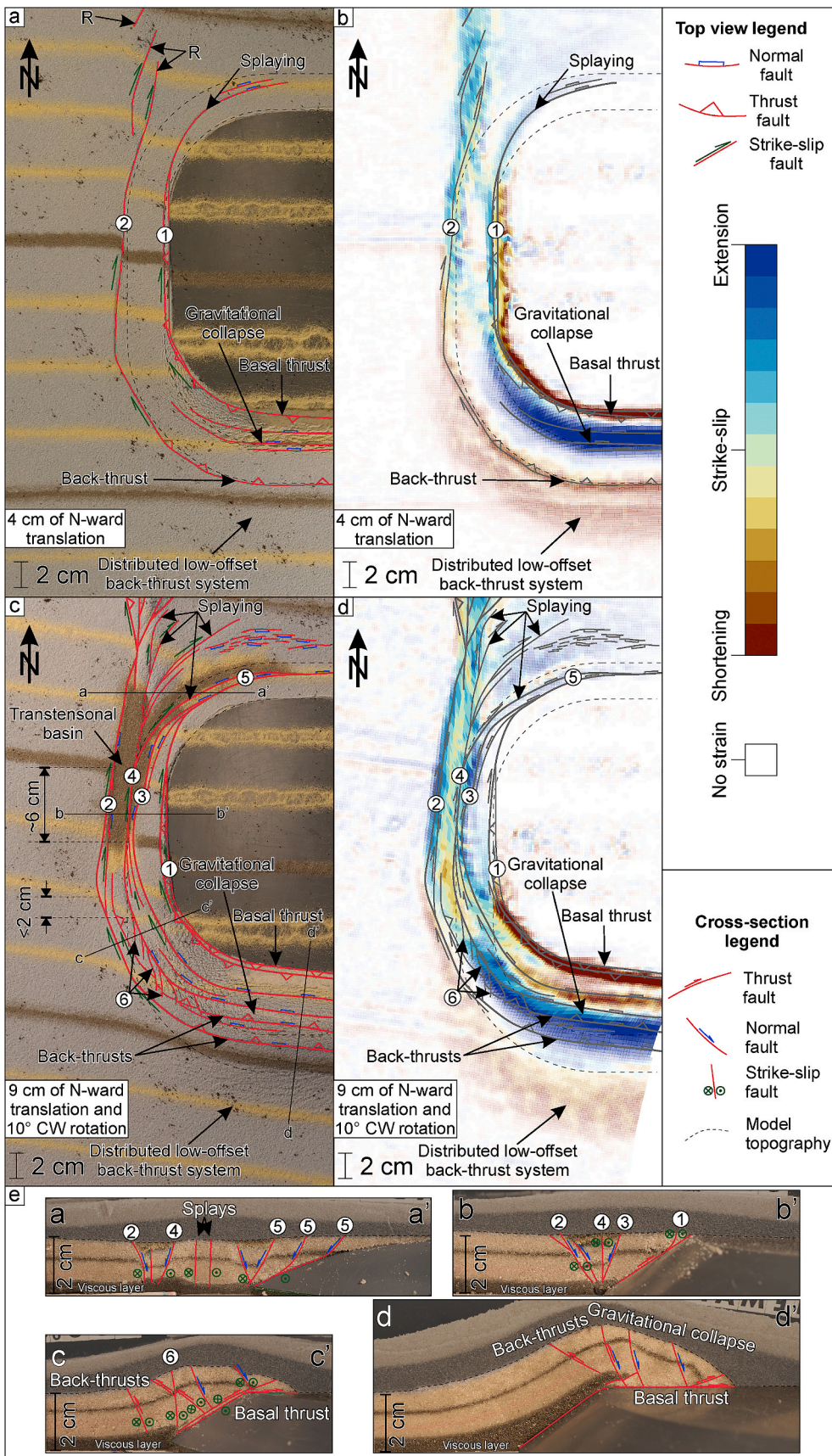
Fig. 8. Model 6 – best-fit model. Dashed black lines mark the upper and lower edges of the indenter. R – Riedel shear. a) Interpreted top-view photo at the end of translation phase. b) Cumulative strain type map at the end of translation-only phase. To supress areas without significant deformation, the transparency of areas with a strain magnitude below the 95 percentile is increased. We define the strain magnitude as the maximum, absolute logarithmic principal stretch (i.e., maximum absolute Hencky strains). c) Interpreted top-view photo at the end of the experiment. d) Cumulative strain type map at the end of the experiment, where the deformation is analysed starting in the second phase, without the initial 4 cm of translation (i.e., there is no overprint of the previous strain). Strain plots in Fig. 8b, d are overlain with visually interpreted structures from Fig. 8a, c (grey lines). Strain colour legend corresponds to both Fig. 8b, d. e) Cross-sections of the best-fit model. Dashed line marks the model topography at the end of the experiment. Shaded area in the upper part of each cross-section marks post-kinematic sand cover. Cross-section locations are shown in Fig. 8c. (For interpretation of the references to colour in this figure legend, the reader is referred to the Web version of this article.)

evolution of first-order structural patterns is similar in brittle and brittle-viscous experiments, especially along the western margin of the indenter. The influence of the viscous crust is particularly obvious at the southern and northern margins of the indenter, where the transfer of deformation is more gradual. Also, notably less structures accommodate shortening south of the indenter, while north of the indenter new structures (i.e., splaying off of the main strike-slip zone; Fig. 5) form that do not exist in brittle-only models. Comparing M7 with M10 shows that main the dextral shear zone evolves on top of the velocity discontinuity in M10 and thus at a distance from the boundary between the rigid indenter and the sand layers. This suggests that flow in the viscous layer has a de-localizing affect.

The viscous layer does not have a significant influence on the width of the transtensional basins along the western margin of the indenter, although the basins are slightly larger (especially longer) (Fig. 7a). The viscous layer controls the geometry of the basin (Fig. 7b), allowing the transfer of deformation around the NW corner of the indenter creating oblique-slip normal faults (splaying in Fig. 5d, g, h, k, l, 7b). These oblique-slip faults control the subsidence in this NE-SW to E-W oriented basin north of the indenter, which is connected to the main N–S oriented basin along the western margin (Figs. 5 and 7b).

The orogenic wedge at the southern margin of the indenter is systematically wider but is not systematically different in height for models with viscous rheology (Fig. 6b). The associated faulting patterns is characterized by a few discrete structures (on average 1–2 fore-thrusts and up to 2 back-thrusts) additional to a multitude of low offset structures appearing as "wrinkles" on the model surface (Fig. 5).

5. The best-fit model for the Cerna-Timok system and associated Carpatho-Balkanides oroclinal bending

Among all modelling scenarios (Fig. 5), the one that simulates most closely the evolution and geometry of the Cerna-Timok fault system and the associated oroclinal bending is model 6, hereafter referred as the "best-fit" model. This model consists of a rigid block with rounded corners and a brittle-viscous rheology (Table 1, Fig. 2a, c, f), where kinematic boundary conditions are applied in two stages. After four centimetres of northward translation (i.e., the first stage), a total 10° clockwise rotation is applied simultaneously with continued northward translation (i.e., the second stage). This setup creates a combination of constant translation and rotation of the moving basal plastic sheet (Fig. 2c).

Similar to the previously described ones (Fig. 5), the best-fit model transfers strike-slip and transtension in the west into thrusting in the south via a transpressional region at the SW corner of the indenter (Fig. 8). The viscous layer distributes deformation over a larger area when compared to the reference model, with a similar geometry to the one of the Cerna-Timok faults system (compare Figs. 1c and 8).

The initial translation stage (Fig. 8a and b) forms NNE-SSW oriented en-echelon Riedel shears oblique to the basal VD in the north (R in Fig. 8a) and two main strike-slip faults along the western margin (structures 1 and 2 in Fig. 8a and b), similar to other models (Fig. 5). These strike-slip faults simulate an original onset of the Timok and Cerna as separate faults, which were linked to the main southern thrusting area via the curved SW indenter's corner, in a similar way to the transfer to an initial Cerna-Timok dextral offset to the Balkanides (compare with thrusting in Fig. 1c). This geometry also implies that the present-day truncation of the Cerna by the Timok Fault is a later, early Miocene feature, by a splay connecting the southern Cerna with the northern Timok. The southern area shows distributed low offset back-thrusts (Fig. 8a), while north dipping normal faults accommodate the collapse of the gravitationally unstable thrust wedge in the hinterland of the main thrust front (blue in Fig. 8b).

5.1. Transtensional basin geometry and structure

The transfer of deformation around the NW indenter corner from strike-slip/transtension (green and light blue values in Fig. 8b) along the western margin into transtensional (light blue and pale blue values in Fig. 8b) deformation in the north of the indenter takes place already during the initial translation stage (Fig. 8a and b). Such a transfer mechanism has already been inferred for the general splaying of strike-slip system towards the South Carpathians, around the rigid indenter's NW corner, where the slip changes from strike-slip into oblique normal-slip and even normal-slip deformation, resulting in the early Miocene transtensional opening of the Getic Depression (Fig. 1c, Matenco et al., 2003; Krézsek et al., 2013).

The subsequent rotation in the best-fit model has comparable scaled dimensions and is controlled by 10° of total clockwise rotation along the western margin of the indenter (Fig. 8c), an amount that was reported for the Serbian Carpathians for Oligocene – Miocene times (Marović et al., 2002). In the same area, the model shows the formation of transtensional basins along the western margin of the indenter that are very similar with the ones observed in the natural case (Fig. 1c). The similarity also insinuates that the subsurface SW and NW corner geometry of Moesian indenter had a similar curvature with the one presently observed. In models with rectangular indenters and 10° CW rotation, basins are much larger than the ones observed in the Serbian and South Carpathians (compare Figs. 1c, 5 and 7). The subsequent rotation in the best-fit model complicates the structural pattern by distributing deformation over additional structures. For instance, new faults (e.g., 3 and 4 in Fig. 8c) form in the area between previously formed structures (1 and 2, Fig. 8c and d), similarly to other models with rotation (Fig. 5). Furthermore, rotation increases oblique movements along all structures (intercalating light blue and yellow – orange colours in Fig. 8d).

In more details, the transtensional basin at the western margin of the indenter displays a more complex geometry than the one in the reference model because of the combined influence of the rotation and viscous layer at the bottom. In M6 it consists of two interconnected basins (Fig. 8c) which gradually enlarge and connect in later stages of deformation. The larger basin (Figs. 7b and 8c) is elongated in roughly N–S direction and is opened along the western margin of the rigid block. The smaller one is located to the north with a curvature controlled by the NW corner of the indenter.

The geometry of the larger basin is controlled by the position with respect to the pole of rotation (fixed pin in Fig. 2a, c). Initially, a triangular transtensional basin opens due to the oblique normal slip along Riedel shears (similar to M4, M5, M7-10 in Fig. 5), which gradually widens southwards with subsequent deformation and rotation (i.e., in the direction away from the pole of rotation). Transtensional (dextral-normal) faults control the subsidence and bound the basin to the west and east (structures 2 and 3 in Fig. 8c). Structure 2 accommodates a larger amount of deformation (Fig. 8e, cross-sections a-a', b-b'). Its associated sedimentary infill is affected by subsequent dextral strike-slip faulting (structure 4) that cuts through the basin and transfers most offset from structure 2 (Fig. 8c). These modelling geometries are fairly similar with the triangular geometry and differential subsidence observed in the Timok - Knjaževac basins system (Fig. 1c, Marović et al., 2007).

The smaller basin opens along the northern margin and NW curved corner of the indenter. In this area, the transtensional dextral slip is transferred into dominantly NNW- to N-dipping normal faults (structure 5 in Fig. 8c and d and cross-section a-a' in Fig. 8e) that control sedimentation in the basin. The offsets along these faults are significantly smaller than along faults controlling the N–S oriented basin and, therefore, the curved basin in the north is shallower (e.g., cross-section a-a' in Fig. 8e). These transtensional faults form towards the end of the experiment and have eastward decreasing offsets (structure 5 in Fig. 8c and d). These patterns are in agreement with observations in the Getic

Depression (Fig. 1c), where the Timok Fault splays in multiple branches with gradually decreasing offset (e.g., Răbăgia et al., 2011 and references therein). However, the basin that opens along the NW corner and northern margin of the rigid block in the best-fit model is much shallower compared to up to 3 km subsidence generated in the Getic Depression (Matenco et al., 2003). This observation indicates that dragging along the Cerna-Timok faults system may be responsible for the ultimate connection between the Timok basin and the Getic Depression but is not the main mechanism controlling the subsidence in the latter. This is in agreement with the interpretation of the transtensional Getic Depression opening mechanism (e.g., Krézsek et al., 2013; Maţenco, 2017) in response to the Carpathians slab pull (presently remaining only as the Vrancea slab, Fig. 1a) and its associated tearing along an E-W oriented Subduction-Transform Edge Propagator (STEP) system in the South Carpathians (Fig. 1a; Govers and Wortel, 2005; Maţenco, 2017). Our modelling does not account for such more advanced geodynamic effects.

5.2. Transition between strike-slip/transtension and thrusting

South of the N–S oriented basin along the western indenter's margin, the strike-slip deformation is distributed over numerous vertical to high-angle faults (Fig. 8c, e, cross-section c-c'). These faults have a normal slip component that decreases southwards and is replaced with oblique reverse slip as the deformation is gradually transferred around the SW corner of the indenter (Fig. 8c and d) and further to thrusting south of the indenter (Fig. 8c and d, cross-section d-d' in Fig. 8e). The thrusting in the south and associated normal faulting due to the gravitational instability of the built-up wedge (Fig. 8c and d) are similar as in the reference model. The only difference is that back-thrusts and normal faults have smaller offsets in the best-fit model (Fig. 8c and d, cross-section d-d' in Fig. 8e). An interesting feature is that the area of gravitational collapse during translation (blue in Fig. 8b) gets shortened during the subsequent rotation (red and orange area in the hanging wall of the basal thrust in Fig. 8d; see also Supplementary Appendix F). Both, thrusts and normal faults have a curved map-view geometry because they are linked with the strike-slip corridor in the west (Fig. 8c).

The transfer of strike-slip deformation into thrusting simulates very well and is compatible with the transfer of deformation observed from the Cerna-Timok fault system into the western Balkanides thrust wedge (e.g, Schmid et al., 2020). The thrusts in the Balkanides also have a curved geometry due to the dextral drag along the Timok Fault during the transfer of deformation (Fig. 1b and c, see Schmid et al., 2020). Minor back-thrusting is also observed in the Balkanides nappes north of the Sofia basin (Fig. 1c).

The offset along the strike-slip system at the western margin of the rigid block decreases southwards in the best-fit model (from ~6 cm to <2 cm, see the offset of black and yellow marker lines in top view of Fig. 8c). Notably, the southern propagation of the strike-slip faults offset earlier shortening structures (structure 6 in Fig. 8c, e, cross-section c-c'). Such propagation of strike-slip faults and truncation of older structures in the south are common features in other models as well (e.g., fault 6 in M2, 6 and 7 in M3, 6 in M4, southern prolongation of 4 and 5 in M5, 5 in M7, 6 in M8, 6 and 7 in M9, 3 in M10, southern prolongation of 4 in M11 and M12, Fig. 5). The decrease in offset in models explains well the observed significant decrease in Timok fault dextral offset from 65 km in the north to around 5–10 km south of Pirot basin (Fig. 1c). A large part of the Timok dextral offset is taken up by thrusting in the Balkanides (Schmid et al., 2020), while the remainder in the southward prolongation is less constrained. One interpretation assumes that the Timok Fault is an inherited feature that was connected with the Cretaceous strike-slip deformation in the northern Rhodope (Fig. 1a and b, dashed line in Fig. 1c, the connection with the NW-SE oriented Maritsa Fault of Schmid et al., 2020, see also Naydenov et al., 2009, 2013; Henry et al., 2012; Vangelov et al., 2016). Another interpretation suggests that the Timok Fault continues south of the Pirot basin, offsetting the Kusa Vrana

anticline (Fig. 1c, Kräutner and Krstić, 2003; Vangelov et al., 2016; van Hinsbergen et al., 2020). By comparing the geometries and overall evolution (Figs. 1c, 5 and 8), including the observed geometry of strike-slip deformation, our models are more compatible with the second solution.

6. Deformation transfer and oroclinal bending around indenters

In this section we will discuss and compare our modelling results, summarized in Fig. 9, with previous studies.

6.1. Effects of the rigid indenter geometry on the strain partitioning

Our results show that deformation around a rigid indenter with either round or angular corners leads to curved fault systems where thrusting in the shortening domain transitions to strike-slip deformation through a system of oblique slip faults (Fig. 9). This transitional area coincides with the maximum curvature of the fault system. This curvature is gradual in cases of rounded indenter corners, but abrupt in cases of rectangular corners, indicating that stress concentrations at indenter dips control the locus and geometry of deformation. Similar effects have been shown by Luth et al. (2013), where new faults nucleate at indenter dips. Overall, our results are in line with previous analogue modelling studies where the curvature of fold and thrust belts in front of an indenter are controlled by the indenter geometry (Marshak, 1988; Marshak et al., 1992; Zweigel et al., 1998; Costa and Speranza, 2003; Crespo-Blanc and González-Sánchez, 2005; Luth et al., 2013; Jiménez-Bonilla et al., 2020). Similar to our results, these studies exhibit a narrowing of the deformed area when deformation is transferred from the frontal to the lateral indenter margin (e.g., Marshak, 1988; Crespo-Blanc and González-Sánchez, 2005; Luth et al., 2013). The change in deformation regime around the indenter is also associated with a decrease in topography from the contractional to the strike-slip domain, which is gradual in case of a rounded indenter (Fig. 9a) because northward translational component of displacement continuously transfers deformation to the strike-slip domain. This material transfer results in a higher topography farther northward and limits the formation of a wide and deep basin. In contrast, when the corner is rectangular (Fig. 9b), the wedge topography rapidly decreases northwards along a series of normal faults leading to a narrow transition zone (Fig. 9b).

The structure of the thrust wedge that forms south of the indenter is largely independent of the indenter geometry. The top to north basal thrust has a flat-ramp-flat geometry and the south-verging back-thrust system accommodates deformation in the hanging wall during thrusting (Fig. 5, see also cross-sections e-e' in Fig. 3g and d-d' in Fig. 4e). N-dipping normal faults, which reactivate previously formed back-thrusts, are interpreted as an expression of gravitational instability on top of the upper flat segment (Fig. 3g, cross-section e-e', Fig. 4e, cross-section d-d' and Fig. 8e, cross-section d-d'; see also Supplementary Appendix C, F). These key features are consistent with previous modelling studies (Bonini et al., 2000; Rosas et al., 2017 and references therein; Fedorik et al., 2019).

6.2. Rotational control on the coupled basin-orogen evolution

In our models, morphologic depressions with limited lateral extent evolve along the strike-slip shear zone (Fig. 5) and probably reflect early dilatancy during shear zone development. All major sedimentary basins open in response to rotation of the mobile plate (Fig. 9c). During rotation the tangential extension (i.e., pole of rotation coincides with the pole of extensional opening) will create basins with a triangular map-view geometry (Fig. 9c), which is narrowing towards the pole of rotation, as observed in many natural examples including the Aegean (eg. Brun et al., 2016) or the southern Ethiopian segment of the East African rift system (Philippon et al., 2014), and modelling studies (Zwaan et al., 2020 and references therein).
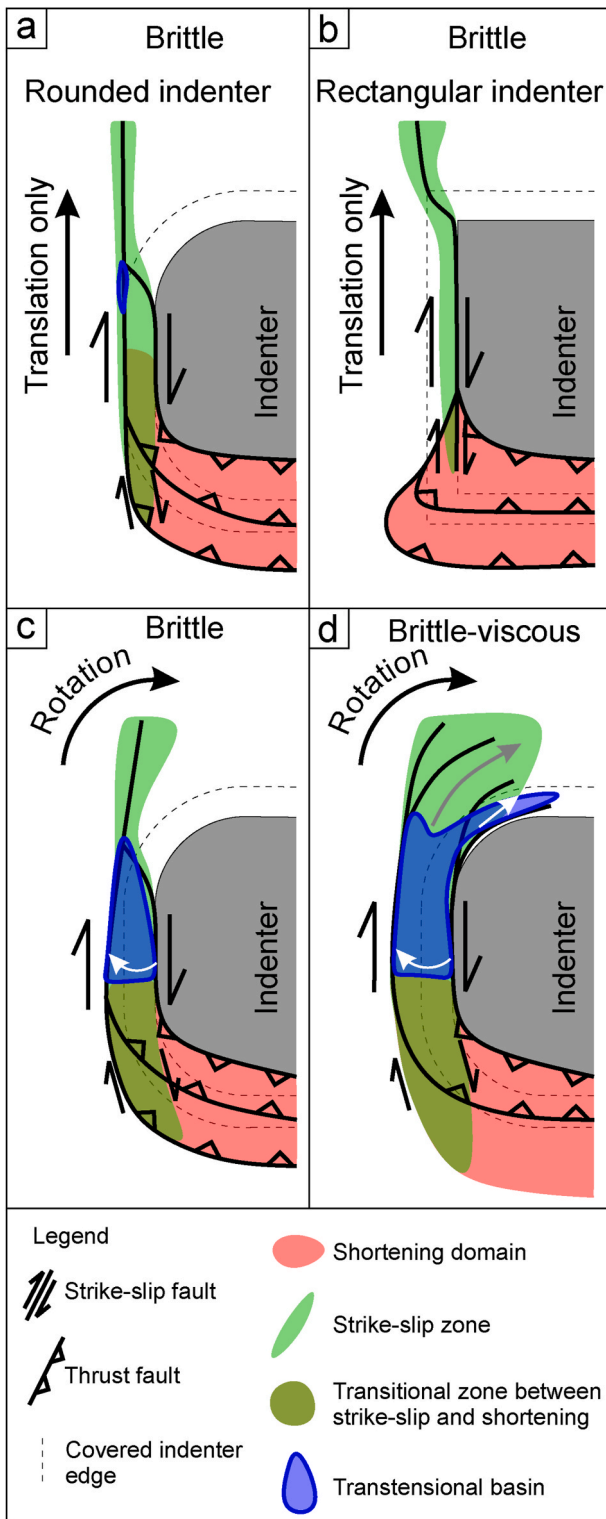
Fig. 9. Influence of various parameters on the structural evolution and deformation transfer around indenter. a) and b) Comparison of effects of different indenter geometries (rounded vs rectangular, respectively) on transfer of deformation between different indenter margins. c) Effects of rotation on widening the deformation zone and opening of triangular basins. White arrow indicates the direction of the basin opening. d) Added effects of flow in the viscous layer compared to brittle only rheology as in Fig. 9c. Viscous layer distributes deformation in a larger area and facilitates transfer of deformation around indenters corners. Grey arrow indicates direction of flow in the viscous layer. White arrow indicates the direction of the basin opening.

Although basins in our models are triangular and overall become narrower northwards (Figs. 5 and 7b), the combination of rotation and translation creates significant dextral shearing within the basin and partitions deformation between normal, oblique-normal and strike-slip faults as also described by Farangitakis et al. (2019; 2021). This is different to rotational extensional settings without coeval translation, where the size of the basin and its propagation towards the pole of rotation is solely controlled by the amount of rotation (Zwaan et al., 2020). The dextral component of shearing inside the basin creates major high angle faults, which are similar to the previous results of transtensional strike-slip experiments invoking a curved velocity discontinuity at the base of the model (Smit et al., 2010).

Shearing along the oblique-slip dextral faults transfers northern parts of the basin beyond of the pole of rotation (Fig. 7b), which would otherwise be an area of transpression (see Zwaan et al., 2020). This effect is enhanced when invoking a ductile crust (see section 6.3). We furthermore note that the geometry of rotational triangular basins can also be controlled by inherited structural patterns or rheological heterogeneities (e.g., Molnar et al., 2017; 2019; Zwaan and Schreurs, 2020). However, as these aspects are not the focus of this study, they will not be discussed further.

6.3. Influence of the viscous layer on structural patterns

The presence of a viscous layer distributes deformation over larger areas with a lower number of high offset structures (Figs. 5–7, 9d). The reduced number of faults in these models and a more gradual transition of deformation along the indenter's margins results in a less well-developed structural pattern. These features have also been observed in previous studies (e.g., Casas et al., 2001; Leever et al., 2011; Luth et al., 2013; Jiménez-Bonilla et al., 2020 and references therein).

A novel aspect of our study is related to the transfer of deformation around the north-western indenter corners, where we interpret the development of splay faults in the brittle layer as an expression of flow in the underlying viscous layer that also affects areas on the adjacent fixed sheet (see Figs. 2c, 7 and 9c). We suggest that this flow generates a transtensional deformation regime leading to minor thinning of the viscous layer and subsidence within a local basin. The geometry of the (sub-)basin is controlled by the geometry of the NW corner (curved basin vs. more angular basin connection, Fig. 7b). South of the indenter, where the viscous layer is involved in thrusting over the ramp, most of the shortening is accommodated by the main basal thrust with well distributed hanging wall shortening (e.g., Fig. 8e, cross-section d-d'), which is also observed in models by Bonini et al. (2000).

7. Conclusions

We present a series of crustal scale analogue experiments studying strain partitioning around an overall rectangular, rigid indenter with inclined margins. The investigated parameters include the shape of the indenter corners, the kinematic boundary conditions and the rheological stratification of the model crust.

Our models show that the shape of the indenter corners (rounded versus rectangular) has a major control on the style and geometry of deformation in the vicinity of the indenter. Styles of deformation include thrusts striking parallel to the indenter margin in the contractional domain, strike-slip fault systems parallel to the overall transport direction and oblique slip fault systems accommodating the deformation transfer from the contractional to the strike-slip domain. Together these structures define an orocline whose curvature, width of deformed area and along strike topographic gradient are largely controlled by the indenter corners. Models with rounded corners result in a gradual transition from thrusting to strike-slip deformation affecting a relatively wide area. This transition is abrupt in the case of rectangular indenter corners and deformation is concentrated in the strike-slip domain within a narrow zone close to the indenter-model interface. These

differences are the consequence of stress concentrations at indenter tips.

The modelling results furthermore demonstrate that 10° clockwise rotation of the model layers relative to the stationary indenter is critical for opening of syn-tectonic sedimentary basins with triangular geometry along indenter margin(s). Overall, this area is characterized by transtensional strain where new, steeply dipping strike slip faults with normal component of shear form in the centre of the basin accommodating its rotational opening. Implementation of a viscous layer leads to distribution deformation over a wider area, which is, however, accommodated by fewer large-offset structures. Most importantly, flow of the viscous layer around indenter corner allows for transfer of deformation from the mobile to the stationary plate and the formation of curved transtensional basins.

Based on these models, we propose that oroclinal bending of the Carpatho-Balkanides is not only accommodated by the Cerna and Timok strike-slip faults, but involves the transfer of strain from the Balkanides where simultaneous contraction lead to the formation of a fold and thrust belt. Deformation is partitioned along numerous structures that control the northward translation and coeval opening of the transtensional basins (such as Timok and Knjaževac basins) along the Timok Fault, while the dextral splay faults around the NW Moesian corner, link up with deformation in the Getic Depression. Furthermore, we suggest that the southward decrease in dextral offset along the Timok Fault is a result of deformation transfer into thrusting in front of Moesia, which gradually reduces the amount of strike-slip deformation southwards along this fault.

In general, our modelling results show that oroclinal bending around rigid indenters is inevitably associated with the partitioning of deformation involving the coeval displacement of linked thrust, oblique-slip and strike slip fault systems to accommodate translational and rotational plate movements.

CRediT authorship contribution statement

Nemanja Krstekanić: Conceptualization, Methodology, Validation, Formal analysis, Investigation, Data curation, Writing – original draft, Writing – review & editing, Visualization. **Ernst Willingshofer:** Conceptualization, Methodology, Validation, Resources, Writing – original draft, Writing – review & editing, Supervision. **Taco Broerse:** Methodology, Software, Formal analysis, Data curation, Writing – review & editing. **Liviu Matenco:** Writing – original draft, Writing – review & editing, Supervision. **Marinko Toljić:** Supervision, Writing – review & editing. **Uros Stojadinovic:** Supervision, Writing – review & editing.

Declaration of competing interest

The authors declare that they have no known competing financial interests or personal relationships that could have appeared to influence the work reported in this paper.

Acknowledgements

Appendix A. Supplementary data

Supplementary data to this article can be found online at https://doi.org/10.1016/j.jsg.2021.104386.

Data availability

All raw unprocessed data related to this study are deposited in the Yoda data repository system of Utrecht University with the DOI number https://doi.org/10.24416/UU01-8TX6RL. Further information is available by contacting the corresponding author or the TecLab (teclab.geo@uu.nl).

References

Anderson, D.L., 1971. The san Andreas Fault. Sci. Am. 225 (5), 52–68.

Aramijo, R., Meyer, B., Hubert, A., Barka, A., 1999. Westward propagation of the North Anatolian fault into the northern Aegean: timing and kinematics. Geology 27, 267–270.

Balla, Z., 1987. Tertiary palaeomagnetic data for the Carpatho–Pannonian region in the light of Miocene rotation kinematics. Tectonophysics 139, 67–98.

Basile, C., Brun, J.P., 1999. Transtensional faulting patterns ranging from pull-apart basin to transform continental margins: an experimental investigation. J. Struct. Geol. 21, 23–37.

Benesh, N.P., Plesch, A., Shaw, J.H., 2014. Geometry, kinematics, and displacement characteristics of tear-fault systems: an example from the deep-water Niger Delta. AAPG (Am. Assoc. Pet. Geol.) Bull. 98 (3), 465–482.

Berryman, K.R., Beanland, S., Cooper, S., Cutten, H., Norris, R., Wood, P., 1992. The Alpine fault, New Zealand: variation in Quaternary structural style and geomorphic expression. Annalae Tectonicae 6, 126–163.

Berza, T., Drăgănescu, A., 1988. The Cerna–Jiu fault system (South Carpathians, Romania), a major Tertiary transcurrent lineament. DS Inst. Geol. Geofiz. 72– 73, 43–57.

Bojar, A.-V., Neubauer, F., Fritz, H., 1998. Cretaceous to Cenozoic thermal evolution of the southwestern South Carpathians: evidence from fission-track thermochronology. Tectonophysics 297, 229–249.

Bonini, M., Sokoutis, D., Mulugeta, G., Kantrivanos, E., 2000. Modelling hanging wall accommodation above rigid thrust ramps. J. Struct. Geol. 22, 1165–1179.

Broerse, T., Norder, B., Govers, R., Sokoutis, D., Willingshofer, E., Picken, S.J., 2019. New analogue materials for nonlinear lithosphere rheology, with an application to slab break-off. Tectonophysics 756, 73–96.

Broerse, T., Krstekanić, N., Kasbergen, C., Willingshofer, E., 2021. Mapping and classifying large deformation from digital imagery: application to analogue models of lithosphere deformation. Geophys. J. Int. https://doi.org/10.1093/gji/ggab120 ggab120.

Brun, J.-P., 2002. Deformation of the continental lithosphere: insights from brittle-ductile models. Geological Society, London, Special Publications 200, 355–370.

Brun, J.-P., Faccenna, C., Gueydan, F., Sokoutis, D., Philippon, M., Kydonakis, K., Gorini, C., 2016. The two-stage Aegean extension, from localized to distributed, a result of slab rollback acceleration. Can. J. Earth Sci. 53 (11), 1142–1157. https://doi-org.proxy.library.uu.nl/10.1139/cjes-2015-0203.

Boutelier, D., Schrank, C., Regenauer-Lieb, K., 2019. 2-D finite displacements and strain from particle imaging velocimetry (PIV) analysis of tectonic analogue models with TecPIV. Solid Earth 10 (4), 1123–1139.

Carreras, J., Cosgrove, J.W., Druguet, E., 2013. Strain partitioning in banded and/or anisotropic rocks: implications for inferring tectonic regimes. J. Struct. Geol. 50, 7–21.

Casas, A.M., Gapais, D., Nalpas, T., Besnard, K., Román-Berdiel, T., 2001. Analogue models of transpressive systems. J. Struct. Geol. 23, 733–743.

Cembrano, J., González, G., Arancibia, G., Ahumada, I., Olivares, V., Herrera, V., 2005. Fault zone development and strain partitioning in an extensional strike-slip duplex: a case study from the Mesozoic Atacama fault system, Northern Chile. Tectonophysics 400, 105–125.

Chemenda, A.I., Cavalié, O., Vergnolle, M., Boissou, S., Delouis, B., 2016. Numerical model formation of a 3-D strike-slip fault system. Compt. Rendus Geosci. 348, 61–69.

Chen, Z., Burchfiel, B.C., Liu, Y., King, R.W., Royden, L.H., Tang, W., Wang, E., Zhao, J., Zhang, X., 2000. Global Positioning System measurements from eastern Tibet and their implications for India/Eurasia intercontinental deformation. J. Geophys. Res. 105 (B7), 16215–16227.

Christie-Blick, N., Biddle, K.T., 1985. Deformation and basin formation along strike-slip faults. In: Biddle, K.T., Christie-Blick, N. (Eds.), Strike-Slip Deformation, Basin Formation, and Sedimentation. SEPM Spec. Publ. (No. 37). Society of Economic Paleontologists and Mineralogists, Tulsa, OK, pp. 1–34.

Costa, E., Speranza, F., 2003. Paleomagnetic analysis of curved thrust belts reproduced by physical models. J. Geodyn. 36, 633–654.

Crespo-Blanc, A., González-Sánchez, A., 2005. Influence of indenter geometry on arcuate fold-and-thrust wedge: preliminary results of analogue modelling. Geogaceta 37, 11–14.

Csontos, L., Vörös, A., 2004. Mesozoic plate tectonic reconstruction of the Carpathian region. Palaeogeogr. Palaeoclimatol. Palaeoecol. 210, 1–56.

Dahlen, F., Suppe, J., Davis, D., 1984. Mechanics of fold-and-thrust belts and accretionary wedges: Cohesive Coulomb theory. J. Geophys. Res. 89 (B12), 10087–10101.

Davis, D., Suppe, J., Dahlen, F.A., 1983. Mechanics of fold-and-thrust belts and accretionary wedges. J. Geophys. Res. 88 (B2), 1153–1172.

Davy, P., Cobbold, P.R., 1988. Indentation tectonics in nature and experiment, 1. Experiments scaled for gravity. Bull. Geol. Inst. Univ. Uppsala, N. Ser. 14, 129–141.

Davy, P., Cobbold, P.R., 1991. Experiments on shortening of a 4-layer model of the continental lithosphere. Tectonophysics 188, 1–25.

Del Castello, M., Pini, G.A., McClay, K.R., 2004. Effect of unbalanced topography and overloading on Coulomb wedge kinematics: insights from sandbox modeling. J. Geophys. Res. 109, B05405. https://doi.org/10.1029/2003JB002709.

D'el-Rey Silva, L.J.H., de Oliveira, Í.L., Pohren, C.B., Tanizaki, M.L.N., Carneiro, R.C., Fernandes, G.L. de F., Aragão, P.E., 2011. Coeval perpendicular shortenings in the Brasília belt: collision of irregular plate margins leading to oroclinal bending in the Neoproterozoic of central Brazil. J. S. Am. Earth Sci. 32, 1–13.

De Vicente, G., Regas, R., Muñoz-Martín, A., Van Wees, J.D., Casas-Sáinz, A., Sopeña, A., Sánchez-Moya, P., Arche, A., López-Gómez, J., Oláiz, A., Fernandez Lozano, J., 2009. Oblique strain partitioning and transpression on an inverted rift: the Castilian Branch of the Iberian Chain. Tectonophysics 470, 224–242.

Dewey, J.F., Holdsworth, R.E., Strachan, R.A., 1998. Transpression and transtension zones. In: Holdsworth, R.E., Strachan, R.A., Dewey, J.E. (Eds.), Continental Transpressional and Transtensional Tectonics, Special Publications 135. Geological Society, London, pp. 1–14.

Dimitrijevic, M.D. (Ed.), 1994. Geological Atlas of Serbia 1:2.000.000. Seismotectonic and Seismological Map. Republical Foundation for Geological Investigations and Geological Institute GEMINI, Belgrade, 1994.

Dooley, T.P., Schreurs, G., 2012. Analogue modelling of intraplate strike-slip tectonics: a review and new experimental results. Tectonophysics 574–575, 1–71.

Duarte, J.C., Rosas, F.M., Terrinha, P., Gutscher, M.-A., Malavieille, J., Silva, S., Matias, L., 2011. Thrust–wrench interference tectonics in the Gulf of Cadiz (Africa–Iberia plate boundary in the north–east Atlantic): insights from analog models. Mar. Geol. 289, 135–149.

Dufréchou, G., Odonne, F., Viola, G., 2011. Analogue models of second-order faults genetically linked to a circular strike-slip system. J. Struct. Geol. 33, 1193–1205.

Farangitakis, G.-P., Sokoutis, D., McCaffrey, K.J.W., Willingshofer, E., Kalnins, L.M., Phethean, J.J.J., van Hunen, J., van Steen, V., 2019. Analogue modeling of plate rotation effects in transform margins and rift-transform intersections. Tectonics 38, 823–841.

Farangitakis, G.-P., McCaffrey, K.J., Willingshofer, E., Allen, M.B., Kalnins, L.M., van Hunen, J., Persaud, P., Sokoutis, D., 2021. The structural evolution of pull-apart basins in response to changes in plate motion. Basin Res. 33 (2), 1603–1625. https://doi.org/10.1111/bre.12528.

Fedorik, J., Zwaan, F., Schreurs, G., Toscani, G., Bonini, L., Seno, S., 2019. The interaction between strike-slip dominated fault zones and thrust belt structures: insights from 4D analogue models. J. Struct. Geol. 122, 89–105.

Fitch, T.J., 1972. Plate convergence, transcurrent faults, and internal deformation adjacent to Southeast Asia and the western Pacific. J. Geophys. Res. 77 (23), 4432–4460.

Fügenschuh, B., Schmid, S.M., 2005. Age and significance of core complex formation in a very curved orogen: evidence from fission track studies in the South Carpathians (Romania). Tectonophysics 404, 33–53.

Glen, J.M.G., 2004. A kinematic model for the southern Alaska orocline based on regional fault patterns. In: Sussman, A.J., Weil, A.B. (Eds.), Orogenic Curvature: Integrating Paleomagnetic and Structural Analyses: Geological Society of America Special Paper 383. Geological Society of America, Boulder, CO, pp. 161–172.

González, D., Pinto, L., Peña, M., Arriagada, C., 2012. 3D deformation in strike-slip systems: analogue modelling and num erical restoration. Andean Geol. 39 (2), 295–316.

Govers, R., Wortel, M.J.R., 2005. Lithosphere tearing at STEP faults: response to edges of subduction zones. Earth Planet Sci. Lett. 236, 505–523.

Hatem, A.E., Cooke, M.L., Toeneboehn, K., 2017. Strain localization and evolving kinematic efficiency of initiating strike-slip faults within wet kaolin experiments. J. Struct. Geol. 101, 96–108.

Henry, B., Naydenov, K., Dimov, D., Jordanova, D., Jordanova, N., 2012. Relations between the emplacement and fabric-forming conditions of the Kapitan-Dimitrievo pluton and the Maritsa shear zone (Central Bulgaria): magnetic and visible fabrics analysis. Int. J. Earth Sci. 101, 747–759.

Hirth, G., Teyssier, C., Dunlap, W.J., 2001. An evaluation of quartzite flow laws based on comparisons between experimentally and naturally deformed rocks. Int. J. Earth Sci. 90 (1), 77–87.

Hubbert, M.K., 1937. Theory of scale models as applied to the study of geologic structures. GSA Bulletin 48 (10), 1459–1520.

Iancu, V., Berza, T., Seghedi, A., Gheuca, I., Hann, H.-P., 2005. Alpine polyphase tectono metamorphic evolution of the South Carpathians: a new overview. Tectonophysics 410, 337–365.

Iturrieta, P.C., Hurtado, D.E., Cembrano, J., Stanton-Yonge, A., 2017. States of stress and slip partitioning in a continental scale strike-slip duplex: tectonic and magmatic implications by means of finite element modelling. Earth Planet Sci. Lett. 473, 71–82.

Jiménez-Bonilla, A., Crespo-Blanc, A., Balanyá, J.C., Expósito, I., Díaz-Azpiroz, M., 2020. Analog models of fold-and-Thrust wedges in progressive arcs: a comparison with the Gibraltar arc external wedge. Front. Earth Sci. 8, 72. https://doi.org/10.3389/feart.2020.00072.

Kerrich, R., Beckinsale, R.D., Durham, J.J., 1997. The transition between deformation regimes dominated by intercrystalline diffusion and intracrystalline creep evaluated by oxygen isotope thermometry. Tectonophysics 38, 241–257.

Klinkmüller, M., Schreurs, G., Rosenaub, M., Kemnitz, H., 2016. Properties of granular analogue model materials: a community wide survey. Tectonophysics 684, 23–38.

Krantz, R.W., 1991. Measurements of friction coefficients and cohesion for faulting and fault reactivation in laboratory models using sand and sand mixtures. Tectonophysics 188, 203–207.

Kräutner, H.G., Krstić, B., 2002. Alpine and pre-alpine structural units within southern Carpathians and the eastern Balkanides. In: Proceedings of XVII Congress of Carpathian–Balkan Geological Association, vol. 53. Special Issue.

Kräutner, H.G., Krstić, B., 2003. Geological Map of the Carpatho–Balkanides between Mehadia, Oravița, Niš and Sofia. Geoinstitute, Belgrade. Krézsek et al., 2013.

Kreemer, C., Blewitt, G., Klein, E.C., 2014. A geodetic plate motion and global strain rate model. G-cubed 15 (10), 3849–3889.

Krézsek, C., Lăpădat, A., Maţenco, L., Arnberger, K., Barbu, V., Olaru, R., 2013. Strain partitioning at orogenic contacts during rotation, strike-slip and oblique convergence: paleogene–Early Miocene evolution of the contact between the South Carpathians and Moesia. Global Planet. Change 103, 63–81.

Krstekanić, N., Matenco, L., Toljić, M., Mandić, O., Stojadinović, U., Willingshofer, E., 2020. Understanding partitioning of deformation in highly arcuate orogenic systems: inferences from the evolution of the Serbian Carpathians. Global and Planetary Change. https://doi.org/10.1016/j.gloplacha.2020.103361.

Krýza, O., Závada, P., Lexa, O., 2019. Advanced strain and mass transfer analysis in crustal-scale oroclinal buckling and detachment folding analoguemodels. Tectonophysics 764, 88–109.

Leever, K.A., Gabrielsen, R.H., Sokoutis, D., Willingshofer, E., 2011. The effect of convergence angle on the kinematic evolution of strain partitioning in transpressional brittle wedges: insight from analog modeling and high-resolution digital image analysis. Tectonics 30, TC2013. https://doi.org/10.1029/2010TC002823.

Le Guerroué, E., Cobbold, P.R., 2006. Influence of erosion and sedimentation on strike-slip fault systems: insights from analogue models. J. Struct. Geol. 28, 421–430.

Limberger, J., Calcagno, P., Manzella, A., Trumpy, E., Boxem, T., Pluymaekers, M.P.D., van Wees, J-D., 2014. Assessing the prospective resource base for enhanced geothermal systems in Europe. Geoth. Energ. Sci. 2, 55–71.

Limberger, J., van Wees, J.-D., Tesauro, M., Smit, J., Bonté, D., Békési, E., Pluymaekers, M., Struijk, M., Vrijlandt, M., Beekman, F., Cloetingh, S., 2018. Refining the thermal structure of the European lithosphere by inversion of subsurface temperature data. Global Planet. Change 171, 18–47.

Lister, G.S., Williams, P.F., 1983. The partitioning of deformation in flowing rock masses. Tectonophysics 92, 1–33.

Lodolo, E., Menichetti, M., Bartole, R., Ben-Avraham, Z., Tassone, A., Lippai, H., 2003. Magallanes – Fagnano continental transform fault (Tierra del Fuego, southernmost South America). Tectonics 22 (6), 1076.

Luth, S., Willingshofer, E., ter Borgh, M., Sokoutis, D., van Otterloo, J., Versteeg, A., 2013. Kinematic and analogue modelling of the Passier- and Jaufen faults: implications for crustal indentation in the Eastern Alps. Int. J. Earth Sci. 102, 1071–1090.

Malvern, L.E., 1969. Introduction to the Mechanics of a Continuous Medium. Prentice-Hall, Inc., Englewood Cliffs, NJ, p. 713.

Mann, P., 2007. Global catalogue, classification and tectonic origins of restraining and releasing bends on active and ancient strike-slip fault systems. Geological Scociety, London, Special Publications 290, 13–142.

Marovic, M., Djoković, I., Milićević, V., Toljić, M., Gerzina, N., 2002. Paleomagnetism of the late paleogene and neogene rocks of the Serbian Carpatho-balkanides: tectonic implications. Ann. Geol. Peninsule Balk. 64, 1–12.

Marovic, M., Toljić, M., Rundić, Lj, Milivojević, J., 2007. Neoalpine Tectonics of Serbia. Serbian Geological Society, Belgrade.

Marshak, S., 1988. Kinematics of orocline and arc formation in thin-skinned orogens. Tectonics 7, 73–86.

Marshak, S., Wilkerson, M.S., Hsui, A.T., 1992. Generation of curved fold-thrust belts: insights from simple physical and analytical models. In: McClay, K.R. (Ed.), Thrust Tectonics. Chapman & Hall, pp. 83–92.

Márton, E., 2000. The Tisza megatectonic unit in the light of paleomagnetic data. Acta Geol. Hung. 43 (3), 329–343.

Maţenco, L., 2017. Tectonics and exhumation of Romanian Carpathians: inferences from kinematic and thermochronological studies. In: Rădoane, M., Vespremeanu-Stroe, A. (Eds.), Landform Dynamics and Evolution in Romania. Springer Geography. Springer, pp. 15–56.

Matenco, L., Schmid, S., 1999. Exhumation of the Danubian nappes system (South Carpathians) during the Early Tertiary: inferences from kinematic and paleostress analysis at the Getic/Danubian nappes contact. Tectonophysics 314, 401–422.

Matenco, L., Bertotti, G., Cloetingh, S., Dinu, C., 2003. Subsidence analysis and tectonic evolution of the external Carpathian–Moesian Platform region during Neogene times. Sediment. Geol. 156, 71–94.

McClay, K., Bonora, M., 2001. Analog models of restraining stepovers in strike-slip fault systems. AAPG (Am. Assoc. Pet. Geol.) Bull. 85 (2), 233–260.

Molnar, N.E., Cruden, A.R., Betts, P.G., 2017. Interactions between propagating rotational rifts and linear rheological heterogeneities: insights from three dimensional laboratory experiments. Tectonics 36, 420–443. https://doi.org/10.1002/2016TC004447.

Molnar, N.E., Cruden, A.R., Betts, P.G., 2019. Interactions between propagating rifts and linear weaknesses in the lower crust. Geosphere 15, 1617–1640. https://doi.org/10.1130/GES02119.1.

Morley, C.K., 2002. A tectonic model for the Tertiary evolution of strike–slip faults and rift basins in SE Asia. Tectonophysics 347, 189–215.

Morley, C.K., 2013. Discussion of tectonic models for Cenozoic strike-slip fault-affected continental margins of mainland SE Asia. J. Asian Earth Sci. 76, 137–151.

Nabavi, S.T., Alavi, S.A., Mohammadi, S., Ghassemi, M.R., 2018. Mechanical evolution of transpression zones affected by fault interactions: insights from 3D elasto-plastic finite element models. J. Struct. Geol. 106, 19–40.

Naydenov, K., Peytcheva, I., von Quadt, A., Saro, S., Kolcheva, K., Dimov, D., 2013. The Maritsa strike-slip shear zone between Kostenets and Krichim towns, South Bulgaria d structural, petrographic and isotope geochronology study. Tectonophysics 595–596, 69–89.

Naydenov, K., von Quadt, A., Peytcheva, I., Sarov, S., Dimov, D., 2009. U-Pb zircon dating of metamorphic rocks in the region of Kostenets-Kozarsko villages: constraints on the tectonic evolution of the Maritsa strike-slip shear zone. Rev. Bulg. Geol. Soc. 70 (1–3), 5–21.

Neugebauer, J., 1994. Closing-up structures, alternatives to pull-apart basins: the effect of bends in the North Anatolian fault, Turkey. Terra. Nova 6, 359–365.

Panaiotu, C.G., Panaiotu, C.E., 2010. Palaeomagnetism of the upper Cretaceous sânpetru formation (Haţeg basin, South Carpathians). Palaeogeogr. Palaeoclimatol. Palaeoecol. 293, 343–352.

Pătraşcu, S., Panaiotu, C., Şeclăman, M., Panaiotu, C.E., 1994. Timing of rotational motion of Apuseni Mountains (Romania): paleomagnetic data from Tertiary magmatic rocks. Tectonophysics 233, 163–176.

Perinçek, D., Çemen, İ., 1990. The structural relationship between the East Anatolian and Dead Sea fault zones in southeastern Turkey. Tectonophysics 172, 331–340.

Philippon, M., Corti, G., Sani, F., Bonini, M., Balestrieri, M.-L., Molin, P., Willingshofer, E., Sokoutis, D., Cloetingh, S., 2014. Evolution, distribution and characteristics of rifting in southern Ethiopia. Tectonics 33, 485–508. https://doi. org/10.1002/2013TC003430.

Platt, J.P., 1993. Mechanics of oblique convergence. J. Geophys. Res. 98 (B9), 16239–16256.

Popa, M., Munteanu, I., Borleanu, F., Oros, E., Radulian, M., Dinu, C., 2018. Active tectonic deformation and associated earthquakes: a case study – south West Carpathians Bend zone. Acta Geodaetica et Geophysica 53, 395–413.

Răbăgia, T., Matenco, L., Cloetingh, S., 2011. The interplay between eustacy, tectonics and surface processes during the growth of a fault-related structure as derived from sequence stratigraphy: the Govora–Ocnele Mari antiform, South Carpathians. Tectonophysics 502 (1–2), 196–220.

Ramberg, H., 1981. Gravity, Deformation, and the Earth's Crust: in Theory, Experiments, and Geological Application. Academic Press, London, New York.

Ratschbacher, L., Merle, O., Davy, P., Cobbold, P., 1991a. Lateral extrusion in the eastern Alps, Part 1: boundary conditions and experiments scaled for gravity. Tectonics 10 (2), 245–256.

Ratschbacher, L., Frisch, W., Linzer, H.-G., Merle, O., 1991b. Lateral extrusion in the eastern Alps, Part 2: structural analysis. Tectonics 10 (2), 257–271.

Ratschbacher, L., Linzer, H.G., Moser, F., Strusievicz, R.O., Bedelean, H., Har, N., Mogos, P.A., 1993. Cretaceous to Miocene thrusting and wrenching along the central South Carpathians due to a corner effect during collision and orocline formation. Tectonics 12, 855–873.

Rosas, F.M., Duarte, J.C., Neves, M.C., Terrinha, P., Silva, S., Matias, L., Gràcia, E., Bartolome, R., 2012. Thrust-wrench interference between major active faults in the Gulf of Cadiz (Africa-Eurasia plate boundary, offshore SW Iberia): tectonic implications from coupled analog and numerical modelling. Tectonophysics 548–549, 1–21.

Rosas, F.M., Duarte, J.C., Schellart, W.P., Tomás, R., Grigorova, V., Terrinha, P., 2015. Analogue modelling of different angle thrust-wrench fault interference in a brittle medium. J. Struct. Geol. 74, 81–104.

Rosas, F.M., Duarte, J.C., Almeida, P., Schellart, W.P., Riel, N., Terrinha, P., 2017. Analogue modelling of thrust systems: passive vs. active hanging wall strain accommodation and sharp vs. smooth fault-ramp geometries. J. Struct. Geol. 99, 45–69.

Rudolf, M., Boutelier, D., Rosenau, M., Schreurs, G., Oncken, O., 2016. Rheological benchmark of silicone oils used for analog modling of short- and longterm lithospheric deformation. Tectonophysics 684, 12–22.

Săndulescu, M., 1988. Cenozoic tectonic history of the Carpathians. In: Royden, L.H., Horvath, F. (Eds.), The Pannonian Basin, a Study in Basin Evolution, AAPG Memoir, vol. 45. American Association of Petroleum Geologists, Tulsa, OK, pp. 17–25.

Schellart, W.P., Strak, V., 2016. A review of analogue modelling of geodynamic processes: approaches, scaling, materials and quantification, with an application to subduction experiments. J. Geodyn. 100, 7–32.

Schmid, S.M., Bernoulli, D., Fügenschuh, B., Matenco, L., Schefer, S., Schuster, R., Tischler, M., Ustaszewski, K., 2008. The Alpine–Carpathian–Dinaridic orogenic system: correlation and evolution of tectonic units. Swiss J. Geosci. 101, 139–183.

Schmid, S.M., Berza, T., Diaconescu, V., Froitzheim, N., Fügenschuh, B., 1998. Orogen-parallel extension in the southern Carpathians. Tectonophysics 297, 209–228.

Schmid, S.M., Fügenschuh, B., Kounov, A., Matenco, L., Nievergelt, P., Oberhänsli, R., Pleuger, J., Schefer, S., Schuster, R., Tomljenović, B., Ustaszewski, K., van

Hinsbergen, D.J.J., 2020. Tectonic units of the Alpine collision zone between Eastern Alps and western Turkey. Gondwana Res. 78, 308–374.

Senatore, C., Wulfmeier, M., Vlahinić, I., Andrade, J., Iagnemma, K., 2013. Design and implementation of a particle image velocimetry method for analysis of running, gear–soil interaction. J. Terramechanics 50, 311–326.

Smit, J., Brun, J.-P., Cloetingh, S., Ben-Avraham, Z., 2008. Pull-apart basin formation and development in narrow transform zones with application to the Dead Sea Basin. Tectonics 27, TC6018. https://doi.org/10.1029/2007TC002119.

Smit, J., Brun, J.-P., Cloetingh, S., Ben-Avraham, Z., 2010. The rift-like structure and asymmetry of the Dead Sea Fault. Earth Planet Sci. Lett. 290, 74–82.

Stanier, S.A., Blaber, J., Take, W.A., White, D., 2016. Improved image-based deformation measurement for geotechnical applications. Can. Geotech. J 53 (5), 727–739.

Stefanov, Y.P., Bakeev, R.A., 2014. Deformation and fracture structures in strike-slip faulting. Eng. Fract. Mech. 129, 102–111.

Sternai, P., Avouac, J.-P., Jolivet, L., Faccenna, C., Gerya, T., Becker, T.W., Menant, A., 2016. On the influence of the asthenospheric flow on the tectonics andtopography at a collision-subduction transition zones:Comparison with the eastern Tibetan margin. J. Geodyn. 100, 184–197.

Tapponnier, P., Peltzer, G., Le Dain, A., Aramijo, R., Cobbold, P., 1982. Propagating extrusion tectonics in Asia: new insights from simple experiments with plasticine. Geology 10 (12), 611–612.

Tapponnier, P., Peltzer, G., Aramijo, R., 1986. On the mechanics of the collision between India and Asia. In: Coward, M.P., Ries, A.C. (Eds.), Collision Tectonics, vol. 19. Geological Society Special Publication, pp. 115–157.

Thielicke, W., Stamhuis, E.J., 2014. PIVlab – towards user-friendly, affordable and accurate digital particle image velocimetry in MATLAB. J. Open Res. Software 2, e30. https://doi.org/10.5334/jors.bl.

Turcotte, D.L., Schubert, G., 2014. Geodynamics, third ed. Cambridge University Press, Cambridge, United Kingdom, p. 636.

Ustaszewski, K., Schmid, S.M., Fügenschuh, B., Tischler, M., Kissling, E., Spakman, W., 2008. A map-view restoration of the Alpine–Carpathian–dinaridic system for the early Miocene. Swiss J. Geosci. 101, 273–294.

van der Pluijm, B.A., Marshak, S., 2004. Earth Structure: an Introduction to Structural Geology and Tectonics, second ed. W. W. Norton & Company, Inc., New York, p. 656.

van Gelder, I.E., Willingshofer, E., Sokoutis, D., Cloetingh, S.A.P.L., 2017. The interplay between subduction and lateral extrusion: a case study for the European Eastern Alps based on analogue models. Earth Planet Sci. Lett. 472, 82–94.

Vangelov, D., Pavlova, M., Gerdjikov, I., Kounov, A., 2016. Timok fault and Tertiary strike-slip tectonics in part of western Bulgaria. Annual of the University of Mining and Geology "St. Ivan Rilski" 59 (1), 112–117.

van Hinsbergen, D.J.J., Dupont-Nivet, G., Nakov, R., Oud, K., Panaiotu, C., 2008. No significant post-Eocene rotation of the Moesian Platform and Rhodope (Bulgaria): implications for the kinematic evolution of the Carpathian and Aegean arcs. Earth Planet Sci. Lett. 273, 345–358.

van Hinsbergen, D.J.J., Torsvik, T.H., Schmid, S.M., Maţenco, L.C., Maffione, M., Vissers, R.L.M., Gürer, D., Spakman, W., 2020. Orogenic architecture of the Mediterranean region and kinematic reconstruction of its tectonic evolution since the Triassic. Gondwana Res. 81, 79–229.

van Unen, M., Matenco, L., Demir, V., Nader, F.H., Darnault, R., Mandić, O., 2019. Transfer of deformation during indentation: inferences from the post-middle Miocene evolution of the Dinarides. Global Planet. Change 182, 103027.

Wallace, R.E. (Ed.), 1990. The San Andreas Fault System, California. USGS Professional Paper 1515. US Geological Survey, California.

Wang, H., Liu, M., Ye, J., Cao, J., Jing, Y., 2017. Strain partitioning and stress perturbation around stepovers and bends of strike-slip faults: numerical results. Tectonophysics 721, 211–226.

Weijermars, R., Schmeling, H., 1986. Scaling of Newtonian and non-Newtonian fluid dynamics without inertia for quantitative modelling of rock flow due to gravity (including the concept of rheological similarity). Phys. Earth Planet. In. 43, 316–330.

Willingshofer, E., Sokoutis, D., Beekman, F., Schönebeck, J.-M., Warsitzka, M., Rosenau, M., 2018. Ring shear test data of feldspar sand and quartz sand used in the Tectonic Laboratory (TecLab) at Utrecht University for experimental Earth science applications. GFZ Data Services. https://doi.org/10.5880/fidgeo.2018.072.

Xiao, Y., Wu, G., Lei, Y., Chen, T., 2017. Analogue modeling of through-going process and development pattern of strike-slip fault zone. Petrol. Explor. Dev. 44 (3), 368–376.

Zwaan, F., Schreurs, G., 2020. Rift segment interaction in orthogonal and rotational extension experiments: implications for the large-scale development of rift systems. J. Struct. Geol. 140, 104119. https://doi.org/10.1016/j.jsg.2020.104119.

Zwaan, F., Schreurs, G., Rosenau, M., 2020. Rift propagation in rotational versus orthogonal extension: insights from 4D analogue models. J. Struct. Geol. 135, 103946. https://doi.org/10.1016/j.jsg.2019.103946.

Zweigel, P., Ratschbacher, L., Frisch, W., 1998. Kinematics of an arcuate fold-thrust belt: the southern Eastern Carpathians (Romania). Tectonophysics 297, 177–207.